T.C.
İSTANBUL KÜLTÜR UNIVERSITY
INSTITUTE OF GRADUATE STUDIES

THE EFFECTS OF PLASTIFICATIONS ON VIBRATION CHARACTERISTICS AND STABILITY

MASTER OF SCIENCE THESIS

Abdul Aziz EIN LAROUZI

1800005032

Department: Civil Engineering

Program: Structural Engineering

Supervisor: prof. Dr. Erdal COŞKUN

JUNE 2025

T.C.
İSTANBUL KÜLTÜR UNIVERSITY
INSTITUTE OF GRADUATE STUDIES

THE EFFECTS OF PLASTIFICATIONS ON VIBRATION CHARACTERISTICS AND STABILITY

MASTER OF SCIENCE THESIS

Abdul Aziz EIN LAROUZI

1800005032

Supervisor and Chairperson: prof. Dr. Erdal COŞKUN

Members of Examining Committee: prof. Dr. Faruk KARADOĞAN

prof. Dr. Nazife Özge FERCAN

JUNE 2025

PREAMBLE

I extend my heartfelt gratitude to Istanbul Kültür üniversitesi for the invaluable support, resources, and opportunities provided throughout my academic journey. I am deeply thankful to my professors and committee members for their guidance, encouragement, and expertise, which have been pivotal in shaping this work. Special thanks go to my peers for their collaboration and insightful discussions. Lastly, I am profoundly grateful to my family for their unwavering support, patience, and belief in me, without which this accomplishment would not have been possible. This thesis is a testament to the collective efforts and inspiration of all these contributors.

June 2025 Abdul Aziz EIN LAROUZI

TABLE OF CONTENTS

LIST OF TABLES

LIST OF FIGURES

LIST OF SYMBOLS

f_{syk}	: Characteristics Steel Yield Stress
f_{su}	: Steel Ultimate Stress
E_s	: Steel Modulus of Elasticity
f_{ck}	: Characteristics Concrete Yield Stress
f_{ctk}	: Characteristics Concrete Yield Stress
E_c	: Concrete Modulus of Elasticity
f_c	: Mander Confined Concrete, Concrete Compressive Stress
f_{cc}	: Mander Confined Concrete strength
f_{co}	: Unconfined Concrete Compressive strength
f_e	: Effective Confinement Compression
f_{ex}	: Effective Confinement Compression on X Direction
f_{ey}	: Effective Confinement Compression on Y Direction
f_{ew}	: Stirrups Yield Stress
ρ_x	: Volumetric stirrups ratio on X Direction
ρ_y	: Volumetric stirrups ratio on Y Direction
k_e	: Confinement Effectiveness Factor
a_i	: Distance Between Longitudinal Reinforcement Centers
b_0	: Width of Concrete Between Longitudinal Reinforcement Centres
h_0	: Height of Concrete Between Longitudinal Reinforcement Centres
s	: Distance between stirrups
A_s	: Area of Longitudinal Reinforcement
ε_c	: Concrete Compressive Unit Deformation
ε_{co}	: Unconfined Concrete Yield Strain
f_s	: Reinforcement Steel Stress
ε_s	: Reinforcement Steel Where Strain-Hardening Start
f_{sy}	: Reinforcement Steel Yield Stress
f_{su}	: Reinforcement Steel Ultimate Stress
ε_{su}	: Reinforcement Steel Ultimate Strain
b	: Sections Width

h	: Section Height
L_p	: Plastic Hinge Length From Member End
K	: Stiffness
ω_n	: Natural Circular Frequency
T_n	: Natural Period
M	: Mass
Φ	: Mode Shape
Γ	: Participation Factor
K_{II}	: Second Order Stiffness
V_{tE}^{X}	: Toal Equivalent Seismic Base Shear Force
m_t	: Structures Total Mass
S_{aR}	: Reduced Horizontal Seismic Spectral Acceleration
T_P^X	: Dominant Natural Period of Structure in X Direction
I	: Building Importance Factor
S_{DS}	: Short Period of Horizontal Seismic Spectral Acceleration Factor
S_{ae}	: Horizontal Elastic Spectral Acceleration
R_a	: Earthquake Load Reduction Factor depending on the predicted ductility capacity and period
R	: Structural System Behaviour Factor
ΔF_{NE}^{X}	: Top Roof Additional Shaer Force
F_{iE}^{X}	: Shear Force at Specific Level
D	: Excess Resistance Factor

Enstitüsü: Lisansüstü Eğitim Enstitüsü
Dalı: İnşaat Mühendisliği
Programı: Yapı (İngilizce)
Tez Danışmanı: Dr. Öğretim Üyesi Erdal COŞKUN
Tez Türü ve Tarihi: Yükseklisans – Haziran 2025

KISA ÖZET

KALICI ŞEKIL DEĞIŞTIRMELERIN YAPININ TITREŞIM ÖZELLIKLERI VE STABILITESINE ETKILERI

Abdul Aziz Ein Larouzi

Bu tez, bir betonarme iki boyutlu yapının kapasite eğrileri ile temel periyot ve mod şekilleri gibi serbest titreşim parametrelerini, denge yükleri (ikinci mertebe etkileri) dikkate alarak karşılaştırmalı bir çalışma sunmaktadır. Analiz edilen çerçeve, x yönünde üç açıklık, y yönünde beş açıklık ve beş kattan oluşan bir betonarme binadan türetilmiştir. Bina, TS500 ve TBDY2018 standartlarına uygun olarak tasarlanmıştır. Kapasite eğrileri, kat kütlesi ve mutlak yükseklik, birinci mod şekli, tek modlu modal katkı ve iki modlu modal katılım olmak üzere dört farklı yatay yük dağılımı altında, ETABS yazılımı kullanılarak elde edilmiştir. Serbest titreşim analizi, her mafsal oluşumunda gerçekleştirilmiştir. Tüm dört durumda, temel periyot genellikle her mafsal oluşumunda artış göstermiş, buna karşın denge yükü parametresi, kırılma anında sıfıra ulaşana kadar kademeli olarak azalmıştır. Katılım faktörleri, analiz boyunca önemli bir değişiklik göstermemiştir. Yük dağılımları arasında, kat kütlesi ve mutlak yükseklik temelli yöntem, mod şekillerinde en büyük değişimi göstermiştir. Birinci mod şekli ve tek modlu modal katkı temelli dağılımlar benzer sonuçlar üretirken, iki modlu modal katılım yük dağılımı, alt katlarda bir tarafa ve üst katlarda diğer tarafa kayma şeklinde belirgin bir değişim göstermiştir. Ayrıca, burkulmaya karşı güvenlik faktörü, yatay yük parametresindeki artışa kıyasla daha belirgin bir azalma sergilemiş ve bu durum, basınç kuvvetleri altında burkulma nedeniyle erken kırılmaya yol açabilme potansiyeline işaret etmiştir.

Anahtar sözcükler: Serbest Titreşim Analizi, Mod Şekilleri, Plastik Mafsallar, Artımsal Yük Analizi, Sismik Performans, Yatay Yük Dağılımı

University: İstanbul Kültür University
Institute: Institute of Applied Sciences
Department: Civil Engineering
Program: Structural Engineering
Supervisor: Asst. Prof. ERDAL COŞKUN
Degree Awarded and Date: MA – JUN 2025

ABSTRACT

THE EFFECTS OF PLASTIFICATIONS ON VIBRATION CHARACTERISTICS AND STABILITY

Abdul Aziz Ein Larouzi

This thesis presents a comparative study examining the capacity curves of a reinforced concrete two-dimensional structure, as well as various free vibration parameters, including the fundamental period and mode shapes, while accounting for stability loads (second-order effects). The analyzed frame is derived from a reinforced concrete building with three bays in the x-direction, five bays in the y-direction, and five stories. The building was designed in accordance with TS500 and TBDY2018 standards. The capacity curves were obtained under four different lateral force distributions: based on story mass and absolute elevation, first mode shape, single-mode modal contribution, and two-mode modal participation, utilizing ETABS software. Free vibration analysis was conducted at each hinge occurrence. In all four cases, the fundamental period generally increased with each hinge occurrence, whereas the stability load parameter decreased progressively until reaching zero at failure. The participation factors did not exhibit significant changes throughout the analysis. Among the force distributions, the method based on story mass and absolute elevation demonstrated the largest shift in mode shapes. The distributions based on the first mode shape and single-mode modal contribution produced similar results, while the two-mode modal contribution force distribution showed a notable shift: to one side in the lower stories and to the opposite side in the higher stories. Furthermore, the safety factor against buckling exhibited a more pronounced depreciation compared to the increase in the lateral load parameter, potentially leading to early failure due to buckling force

Keywords: Free Vibration Analysis, Mode Shapes, Plastic Hinges, Pushover Analysis, Seismic Performance, Lateral Load Distribution

1. INTRODUCTION

1.1. Introduction

Earthquakes are one of the biggest hazards that structures could face, not only because of the damage to the structure but also because of the risk that human life could face. Earthquakes occur unpredictably when parts of the Earth's crust collapse at seismic faults; the resulting seismic waves transferred through the soil can vary in parameters such as magnitude, depth, fault type, soil condition, and stress accumulation on rocks. Due to the risk's earthquakes impose, multiple methods exist to assess structural performance against seismic excitations, one of which is static non-linear pushover analysis. This method applies incremental lateral forces to examine structural behavior while accounting for geometric and material non-linearity.

Capacity Curves (or Push-Over Curves) are essential for carrying out performance analysis, providing engineers with realistic insights into a structure's potential nonlinear behavior. Structural behavior is significantly affected by plastifications in critical sections. If the plastic hinge concept is valid for the analyzed structure, dynamic characteristics—such as natural periods, modal participation factors, and mode shapes—will change after plastic hinges form during proportional load increments. Consequently, the lateral load distribution along the building's height also shifts. In this research, these changes are evaluated comparatively, emphasizing how hinge formation sequences and stability load parameters influence dynamic response.

Performing free vibration analysis at each hinge occurrence during static pushover analysis offers valuable insights into structural performance during seismic events. This includes tracking changes in natural periods, frequencies, first modal participation factors,

and the effect of hinge sequences on mode shapes, alongside stability load parameters. By integrating these dynamic shifts with nonlinear static results, the study highlights the evolving behavior of reinforced concrete structures under seismic loading.

This thesis provides critical insights into structural stability and dynamic response under earthquakes, focusing on how plastic hinge development and lateral load redistribution impact performance. By comparing different lateral load distributions and their evolution due to nonlinear behavior, the research enhances understanding of building responses during seismic activity. The findings contribute to safer, more resilient seismic design practices by bridging the gap between theoretical assumptions and real-world nonlinear structural behavior.

1.2. Motivation

This study is motivated by the critical need to understand the behavior of reinforced concrete structures during earthquakes, particularly in terms of their stability and dynamic response. Earthquakes present a significant threat to both human lives and infrastructure and figuring how the structure responds to seismic forces is valuable to reach deeper understanding to the structure behavior at each hinge occurrence to obtain more reliable assessment under such event. The study aims to provide insights into the structural response, especially in relation to hinge formation, stability load, and modal participation and other free vibration analysis factors. The findings from this research will contribute to a better understanding of how buildings respond to earthquakes.

1.3. Literature Review

The foundation of static analysis was established by Takeda and Sozen (1970), who developed a conceptual model for predicting reinforced concrete member response using static force-displacement relationships. Gulkan and Sozen (1974) further advanced this work by introducing an equivalent single degree of freedom system approach. Kilar and Fajfar (1996) contributed by proposing a computational procedure for determining base shear-roof displacement relationships in large-scale elements. Habibullah and Pyle (1998) provided practical guidelines for pushover analysis using ETABS, while Krawinkler and Seneviratna (1998) evaluated the method's advantages and limitations. Mert et al. (2008) validated performance assessment for RC buildings using Turkish code, achieving an 82.9% success rate. Abhilash et al. (2009) investigated different lateral load patterns on four-storied RC structures using FEMA 356 and ATC 40 guidelines. Etedali and Irandegani (2015) proposed new lateral load patterns for steel MRFs, while Kulkarni and Babu Narayan (2018) emphasized the importance of sequential hinge formation in analysis outcomes.The theoretical foundation of limit load analysis began with Neal (1977), whose work, The Plastic Methods of Structural Analysis, established systematic approaches to plastic analysis, mathematical frameworks for limit load calculations, and practical applications in structural design. In the 1970s, Zienkiewicz and Taylor (1977) revolutionized structural analysis with The Finite Element Method, introducing robust numerical methods, systematic discretization, and frameworks for handling material nonlinearity. Chen and Han (1988) advanced the field by integrating plasticity theory with engineering practice in Plasticity for Structural Engineers, introducing advanced yield criteria and methods for managing strain hardening. Modern computational approaches began with Cook et al. (2007) in Concepts and Applications of Finite Element Analysis, who introduced advanced formulations, nonlinear analysis guidelines, and error estimation techniques. Belytschko et al. (2014) furthered nonlinear analysis with advanced solution techniques, material models, and geometric nonlinearity.

Newmark and Hall (1975) advanced safety factors with design response spectra and ductility-based reduction factors for nuclear facilities. The Applied Technology Council's ATC-3-06 (1980) revolutionized seismic design with R-factors, performance-based

criteria, and site-specific considerations. Priestley et al. (2007) in Displacement-Based Seismic Design of Structures integrated displacement-based design and performance-level safety factors. Elnashai and Di Sarno (2008) expanded risk-based safety approaches in Fundamentals of Earthquake Engineering. Finally, Chopra (2015) in Dynamics of Structures introduced modern computational techniques and multi-hazard safety factor integration.

2. METHODOLOGY

2.1. Static Load Analysis

The analysis reinforced a concrete 2D frame located at Istanbul, where the real frame is taken from commercial residential building 5 story with 3 spans in x direction and 5 spans in y directions. The static design loads on the structure can be taken by following TS498. Dead loads on the slabs included concrete leveling, concrete piles, concrete plaster, and the self-weight of structural elements. Live loads and the live load reduction factors can be found as per TS498. Earthquake parameters can be taken based on the AFAD report. The importance factor (I) and structure usage class (BKS) can be determined following TBDY2018, while the earthquake design class (DTS) and structure height class (BYS) can be calculated accordingly. The structure behavior factor (R) and over strength factor (D) can be found based on the reinforced concrete design. Design loads can be found using TS500 (Equation 6.3) and TBDY2018 (Section 4.11)

2.2. Material Properties

Linear material properties for concrete and steel can be defined according to TS500 as shown in table 2.1 and 2.2 respectively, incorporating design safety factors. Beam and column dimensions must be designed according TS500 and TBDY2018.

Table 2.1. Rebar Linear Material Property

Material Type	$f_{yk}\ (MPa)$	$f_{su}\ (MPa)$	Modulus of Elasticity E_s (MPa)
S420	420	500	200000

Table 2.2. Concrete Linear Material Property

Material Type	$f_{ck}\ (MPa)$	$f_{ctk}\ (MPa)$	Modulus of Elasticity E_c (MPa)
C25	25	1.8	30000

2.3. Non-Linear Behavior

Nonlinear material properties can be taken as follows:

2.3.1 Concrete Nonlinearity

Modeled as per TBDY2018 (Section 5A.1) and can be shown in figure 2.1. The confined concrete compressive stress the confined concrete compression stress (f_c) is a function of compression unit strain (ε_c).

$$f_c = \frac{f_{cc}\ x\ r}{r - 1 + x^r} \tag{2.1}$$

Confined concrete compression strength (f_{cc}) and unconfined concrete compression strength (f_{co}) has the following relationship

$$f_{cc} = \lambda_c\ f_{co} \tag{2.2}$$

$$\lambda_c = 2.254\sqrt{1 + 7.94\frac{f_e}{f_{co}}} - 2\frac{f_e}{f_{co}} - 1.254 \tag{2.3}$$

Where (f_e) is effective confinement compression which is taken as the average of x in y direction for rectangular sections of (f_{ex}) and (f_{ey})

$$f_{ex} = k_e\ \rho_x\ f_{yw} \tag{2.4}$$

$$f_{ey} = k_e \rho_y f_{yw} \quad (2.5)$$

Where (f_{yw}) is stirrups yield strength while (ρ_x) and (ρ_y) are the volumetric stirrups ratio in the corresponding direction. While (k_e) is the confinement effectiveness factor ratio.

$$k_e = \left(1 - \frac{\sum a_i^2}{6b_0h_0}\right)\left(1 - \frac{s}{2b_0}\right)\left(1 - \frac{s}{2h_0}\right)\left(1 - \frac{A_s}{b_0h_0}\right) \quad (2.6)$$

Where (a_i) the distance between longitudinal reinforcement in sections' perimeter, (b_0) and (h_0) are the left dimension between stirrups axes while (s) is the distance between stirrups' axes along the member and (A_s) is the area of longitudinal reinforcement on the section.

The relationships for the normalized concrete unit strain in Equation (5A.1) with respect to the variables (x) and (r) are

$$x = \frac{\varepsilon_c}{\varepsilon_{cc}} \quad (2.7)$$

$$f_{ew} = k_e \rho_y f_{yw} \quad (2.8)$$

$$\varepsilon_{cc} = \varepsilon_{co}[1 + 5(\lambda_c - 1)] \quad (2.9)$$

$$\varepsilon_{co} \cong 0.002 \quad (2.10)$$

$$r = \frac{E_c}{E_c - E_{sec}} \quad (2.11)$$

$$E_c \cong 5000\sqrt{f_{co}} \quad (2.12)$$

$$E_{sec} = \frac{f_{cc}}{\varepsilon_{cc}} \quad (2.13)$$

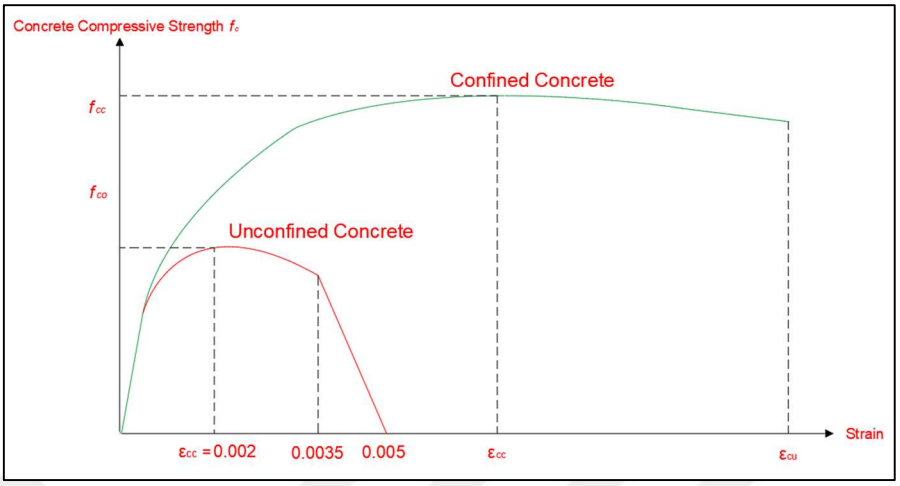

Figure 2.1: Confined and Unconfined Concrete Comparison

2.3.2 Steel Nonlinearity:

Modeled as per TBDY2018 (Section 5A.2) with material property shown in table 2.3 and its stress-strain curve be shown in figure 2.2.

$$f_s = E_s\,\varepsilon_s \qquad (\varepsilon_s \le \varepsilon_y) \qquad (2.14)$$

$$f_s = f_{sy} \qquad (\varepsilon_{sy} < \varepsilon_s \le \varepsilon_{sh}) \qquad (2.15)$$

$$f_s = f_{su} - (f_{su} - f_{sy})\,\frac{(\varepsilon_{su} - \varepsilon_s)^2}{(\varepsilon_{su} - \varepsilon_{sh})^2} \qquad (\varepsilon_{sh} < \varepsilon_s \le \varepsilon_{su}) \qquad (2.16)$$

Table 2.3. Rebar Non-linear Material Property

Type	$f_{sy}\ (MPa)$	ε_{sy}	ε_{sh}	ε_{su}	f_{su}/f_{sy}
S220	220	0.0011	0.011	0.12	1.2
S420	420	0.0021	0.008	0.08	1.15 – 1.35
B420C	420	0.0021	0.008	0.08	1.15 – 1.35
B500C	500	0.0025	0.008	0.08	1.15 – 1.35

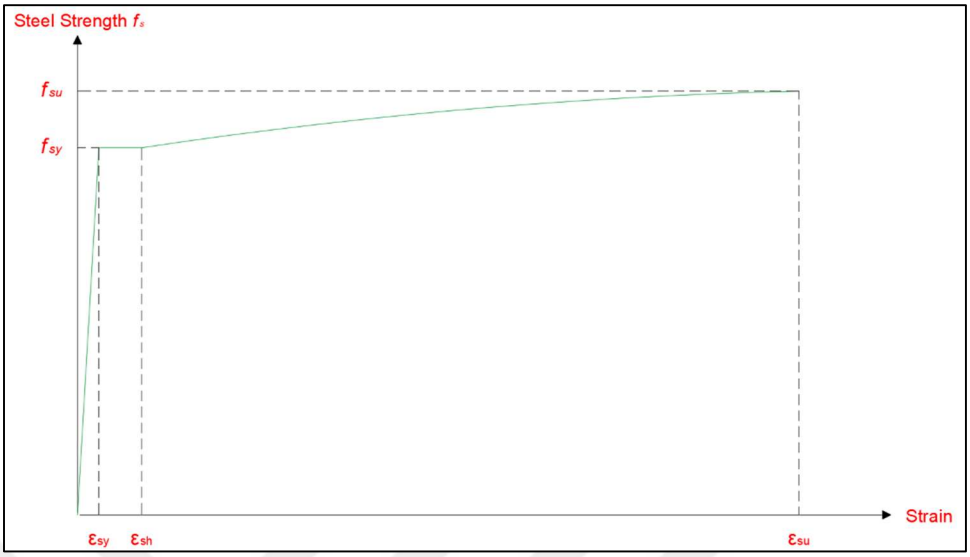

Figure 2.2: Steel Stress-Strain

2.3.3 Geometric Non-linearity

Geometric nonlinearity should be considered in the analysis to account for P−Δ effects, which increase deformation under axial loads. The effect can be shown in figure 2.3

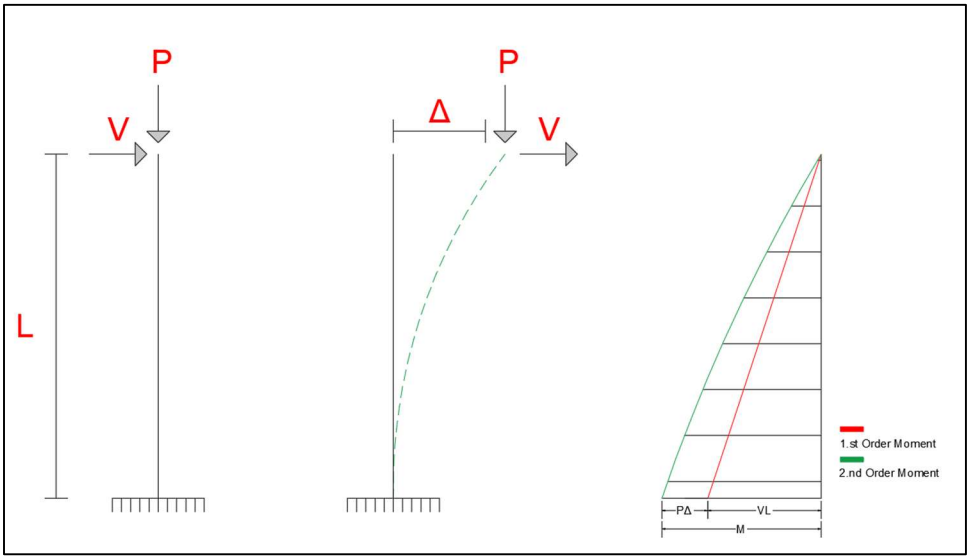

Figure 2.3: Geometrical Non-linearity Effect

2.3.4 Plastic Hinges and Moment-Curvature relationship

The moment-curvature relationships which can be shown in figure 2.4 for each hinge must be calculated, incorporating nonlinear behavior of both concrete and steel. Nonlinear hinges must be assigned at each end of structural members to represent non-linear behavior under incremental lateral loading. The moment-curvature relationship must be taken as P−M3, where axial forces and moments jointly influence the nonlinear response.

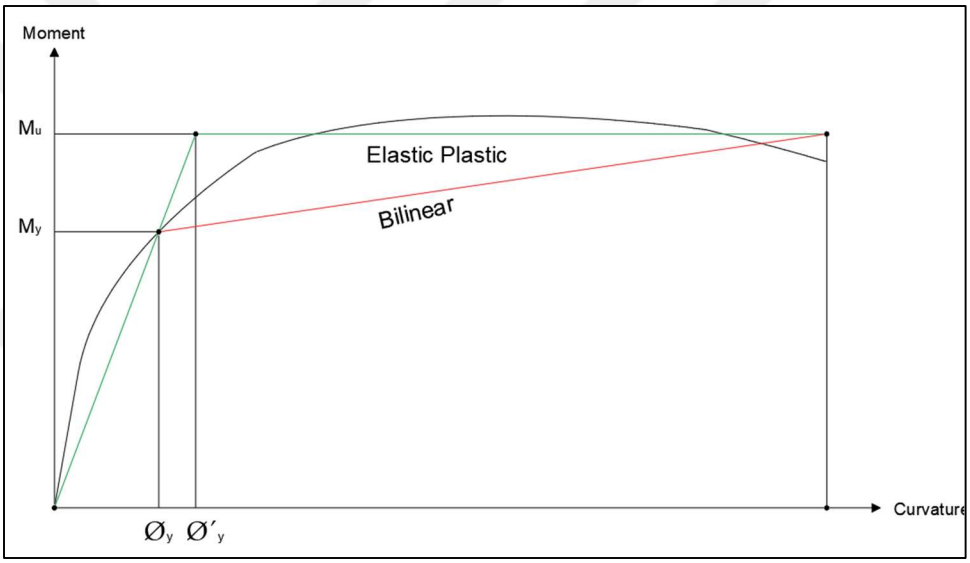

Figure 2.4: Moment-curvature relationship and Bilinearization

The concept of concentrated plasticity which can be shown in figure 2.6 has been used to simulate the non-linear behavior of the element. It assumes the nonlinearity of the members concentrated at both ends at hinge length of the members while the rest of it remains linear. The hinges occur when the internal force of the section exceeds the yield limits, which will reduce its capacity to resist applied forces which can be shown in figure 2.5

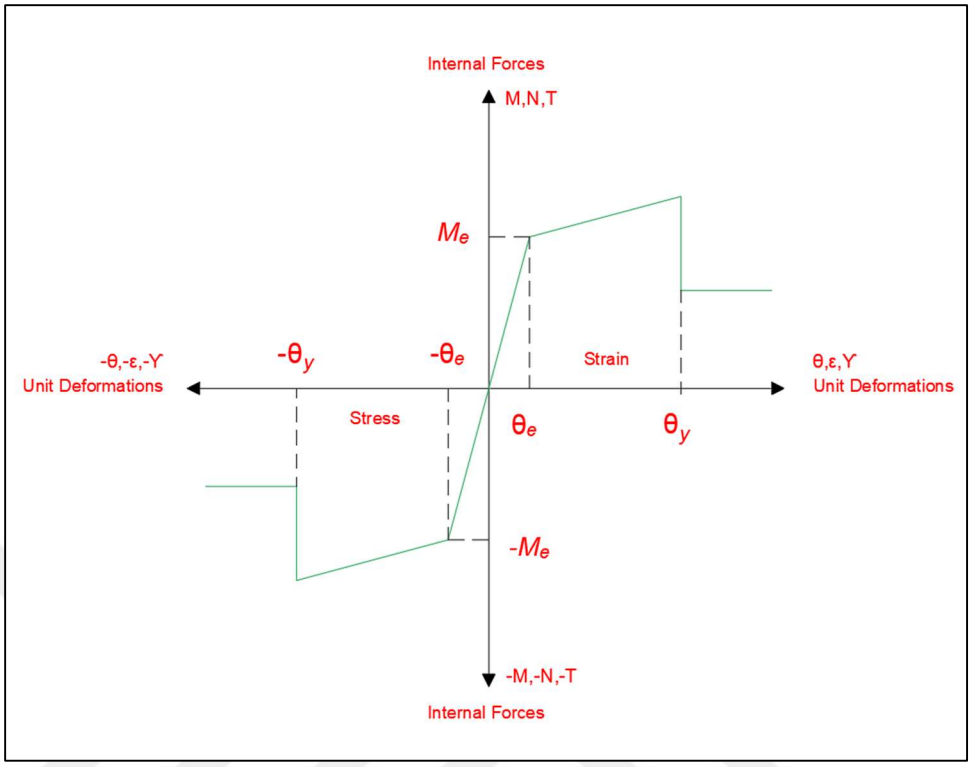

Figure 2.5: Internal Forces of Section

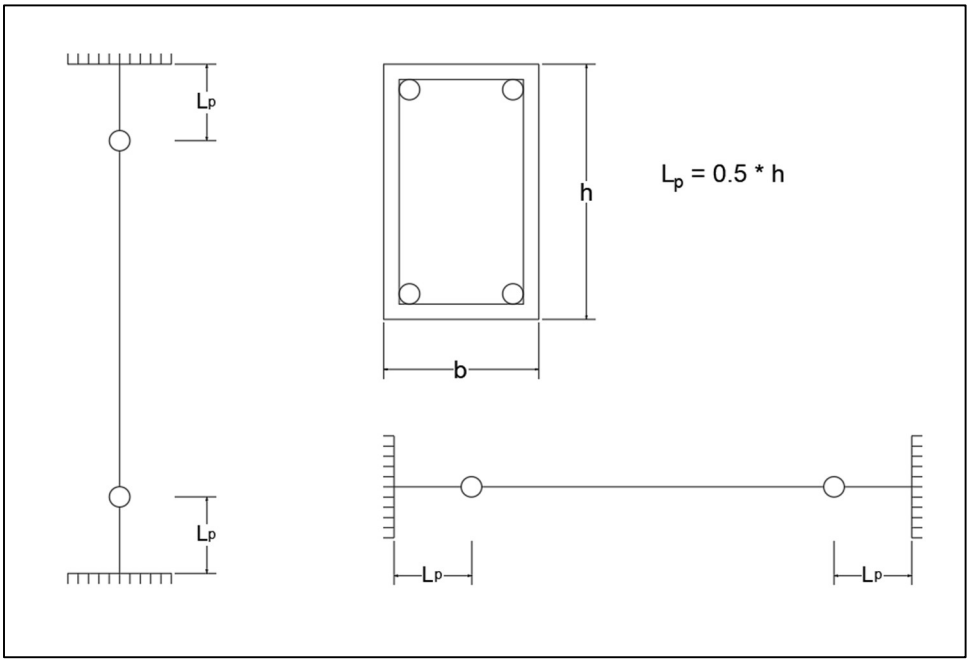

Figure 2.6: Concentrated Plasticity and Hinge Location

2.4. Analysis

2.4.1. Pushover Analysis

Pushover analysis can be used to derive capacity curves for the structure which can be shown in figure 2.7. Lateral forces must incrementally applied until hinges formed. The capacity curve depicted the relationship between the lateral load parameter and top roof displacement at each hinge occurrence.

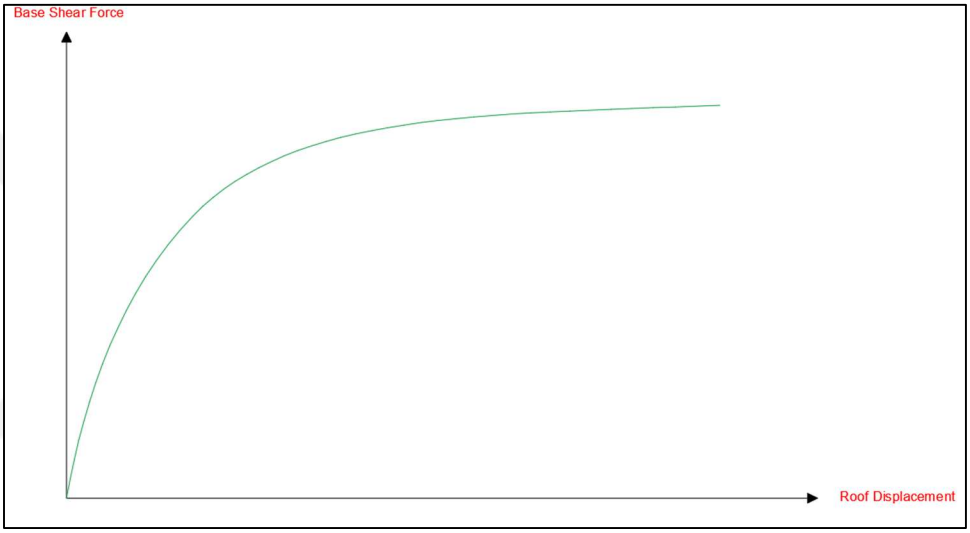

Figure 2.7: Typical Pushover Capacity Curve

2.4.2. Free Vibration Analysis

Free vibration analysis can be at each hinge occurrence to evaluate natural frequencies, mode shapes, and participation factors. These characteristics can be calculated using:

$$\det[k - \omega_n^2 M] = 0 \tag{2.17}$$

$$T_n = \frac{2\pi}{\omega_n} \tag{2.18}$$

$$([k] - \omega_n^2 [M])\{\phi\}_n = \{0\} \tag{2.19}$$

$$\Gamma_i = \{\phi\}_i^T \begin{bmatrix} M_1 \\ M_2 \\ \vdots \\ M_n \end{bmatrix} \tag{2.20}$$

Buckling load parameters can be found from axial forces in columns under the dominant load combination. These must be iteratively, modifying stiffness according to second-order theory as can be shown in figure 2.8 and 2.10 respectively. The critical buckling load can be found by solving:

$$\det [k]_{II} = 0 \tag{2.21}$$

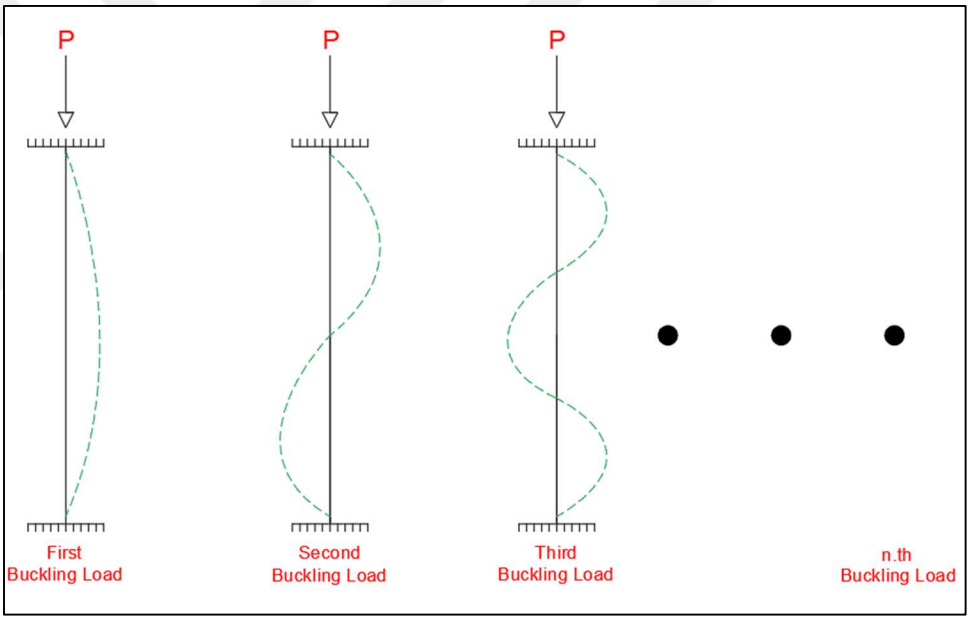

Figure 2.8: Geometrical Non-linearity Buckling Modes

The lumped mass idealization that can be shown in figure 2.9 has been implemented to get the mass matrix which will be used to determine forces and participation ratios.

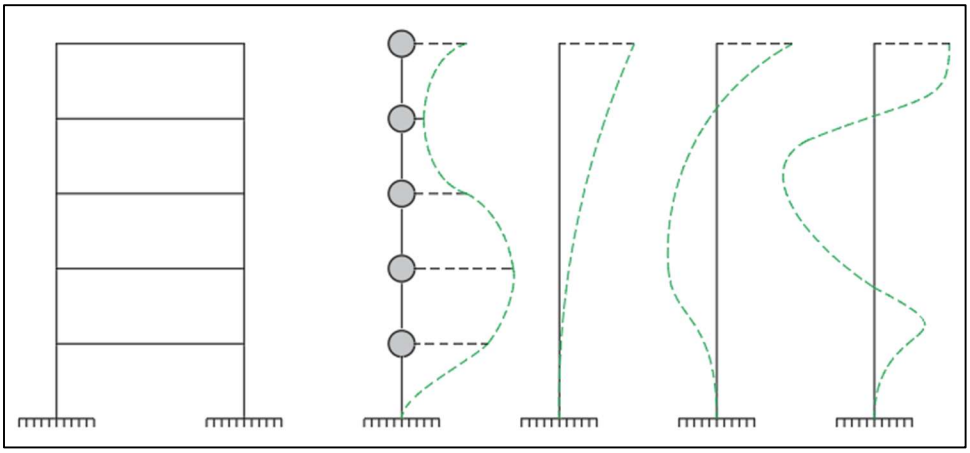

Figure 2.9: Lumped Mass Idealization

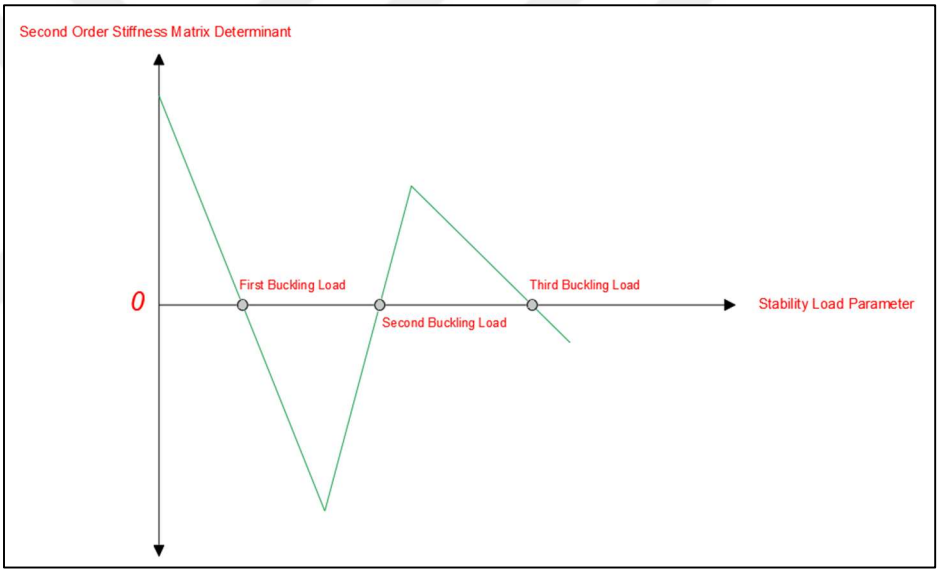

Figure 2.10: Buckling Load Iteration

2.4.3. Lateral Force Distribution

Lateral load distribution along the frame can be categorized into 4 different cases:

Case 1 can be distributed according to mass and absolute which can be shown in figure 2.11

$$V_{tE}^{X} = m_t S_{aR}(T_P^X) \geq 0.04\, m_t\, I\, S_{DS}\, g \qquad (2.22)$$

$$S_{aR} = \frac{S_{ae}}{R_a(T)} \tag{2.23}$$

$$f_s = f_{su} - (f_{su} - f_{sy}) \frac{(\varepsilon_{su} - \varepsilon_s)^2}{(\varepsilon_{su} - \varepsilon_{sh})^2} \tag{2.24}$$

$$R_a(T) = \frac{R}{I} \qquad T > T_B \tag{2.25}$$

$$R_a(T) = D + \left(\frac{R}{I} - D\right) \frac{T}{T_B} \qquad T \leq T_B \tag{2.26}$$

$$m_t = \sum_{i=1}^{N} m_i \tag{2.27}$$

$$V_{tE}^X = \Delta F_{NE}^X + \sum_{i=1}^{N} F_{iE}^X \tag{2.28}$$

$$\Delta F_{NE}^X = 0.0075\, N\, V_{tE}^X \tag{2.29}$$

$$F_{iE}^X = (V_{tE}^X - \Delta F_{NE}^X) \frac{m_i\, H_i}{\sum_{j=1}^{N} m_j\, H_j} \tag{2.30}$$

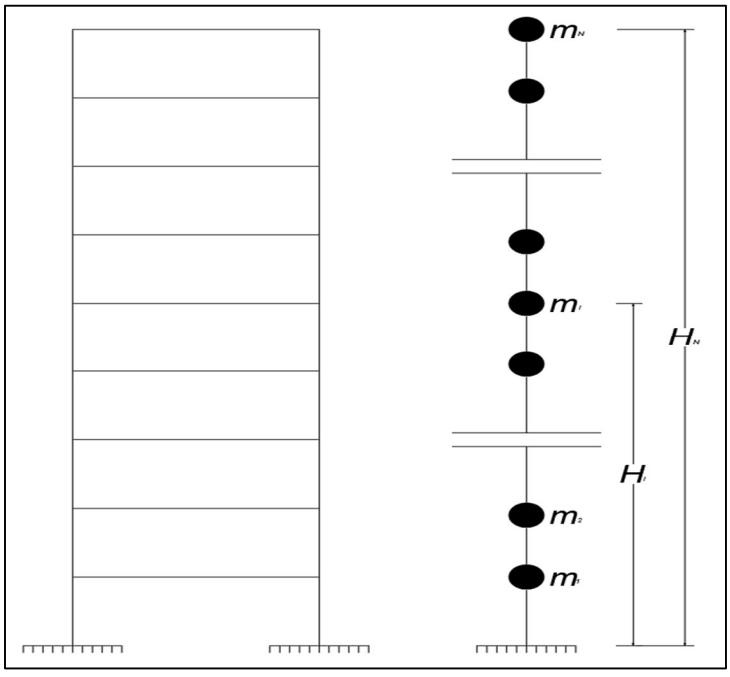

Figure 2.11: Force Distribution According to Equivalent Seismic Force Method

Where in case 2 the lateral forces can be distributed according to the first mode with same base shear force in case 1.

In case 3 the lateral forces can be distributed according to modal contribution taking into consideration only the first mode. While at each hinge occurrence the distribution of forces will be modified according to the new first mode shape and free vibration parameters. Both cases 2 and 3 can be shown in figure 2.12

$$m_{ixn}^{x} = m_i \, \phi_{ixn} \, \Gamma_n^x \tag{2.31}$$

$$F_{iE}^{X} = \sqrt{\sum_{n=1}^{N} (\Gamma_N \, \phi_{iN} \, M \, S_a(T_N))^2} \tag{2.32}$$

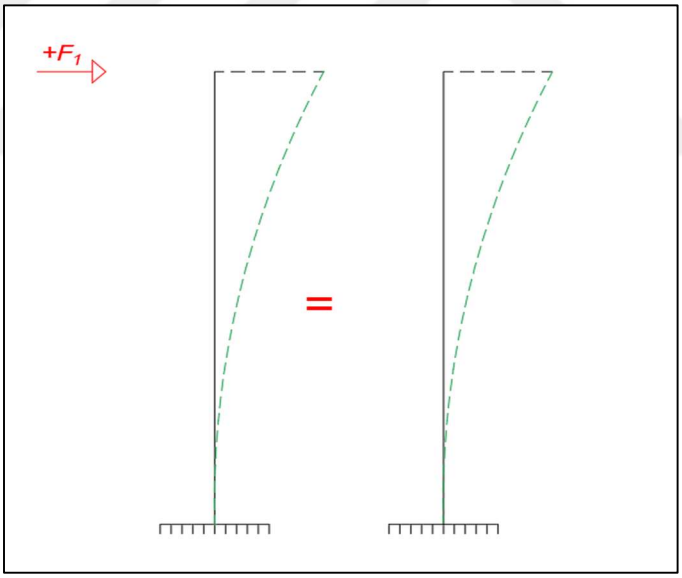

Figure 2.12: Force Distribution According to First Mode

In case 4 similarly to case 3 while taking into consideration 2 mode shapes instead of 1, and it can be shown in figure 2.13

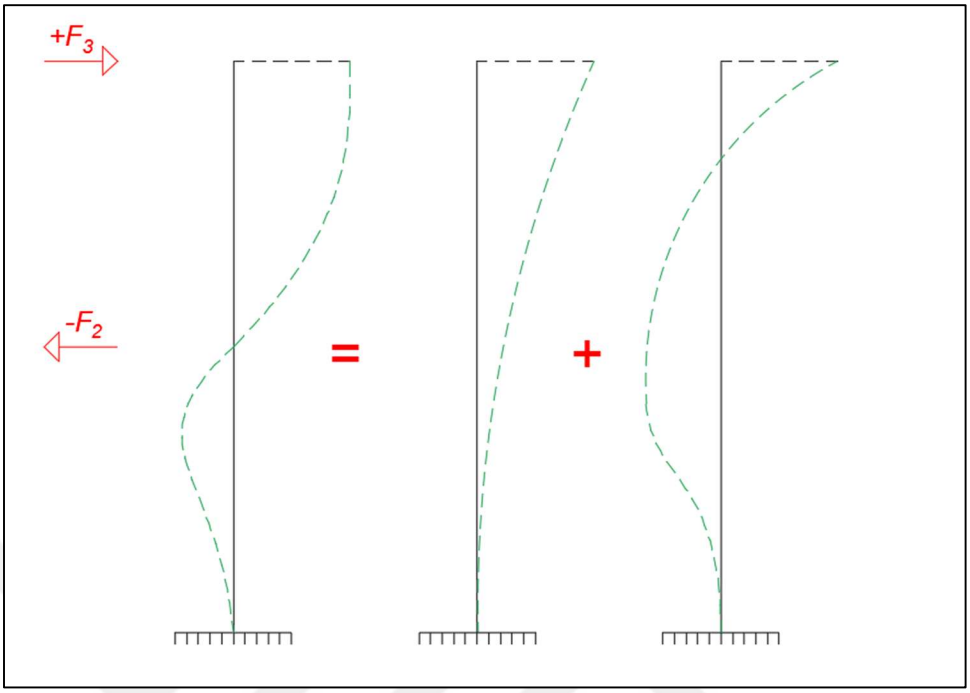

Figure 2.13: Force Distribution According to Two modal

2.5. Software Utilized

XTRACT: Can be used to calculate the moment-curvature relationships of all concrete sections.

ETABS: Can be used for buckling load analysis, pushover analysis, and free vibration analysis.

3. STUDY CASE

3.1. Geometrical and Material Properties

The study case is conducted for reinforced concrete 2D frame located at Istanbul. The real frame is taken from a residential building 5 story with properties as shown below. The study case aims to compare different lateral load distribution patterns effect on the capacity curve of the structure and how sequence of hinge formation can affect the free vibration analysis parameters, and stability load parameter using non-linear static pushover analysis. The structure plane and frame dimension and cross section indices can be shown in figure 3.1 and 3.2 respectively

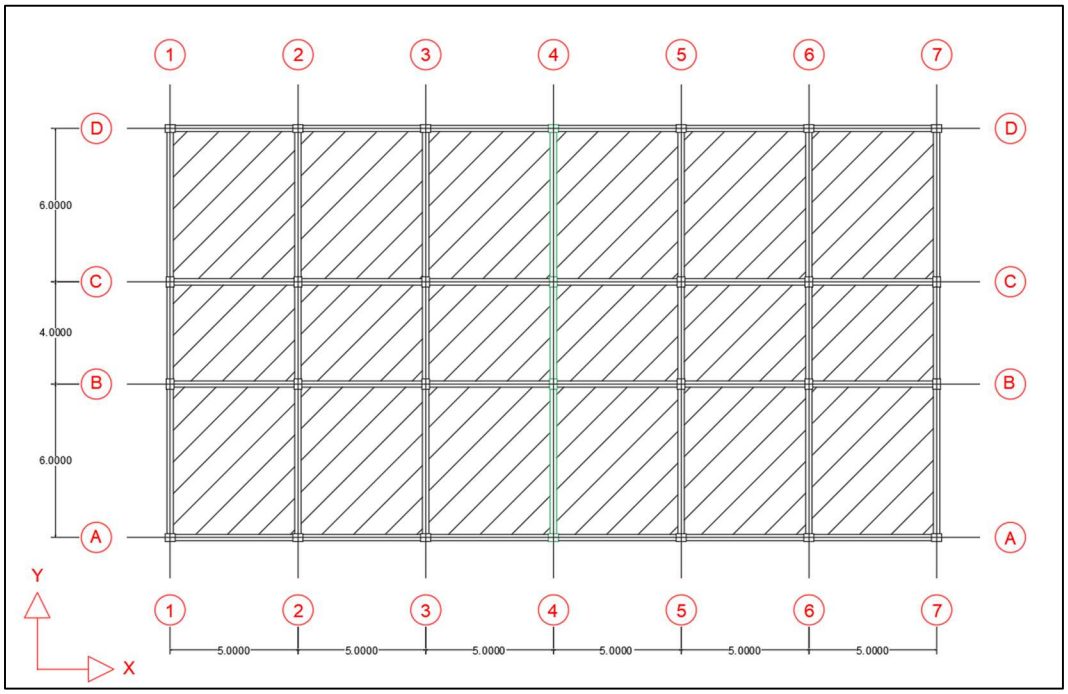

Figure 3.1: Structure Plan and Dimension

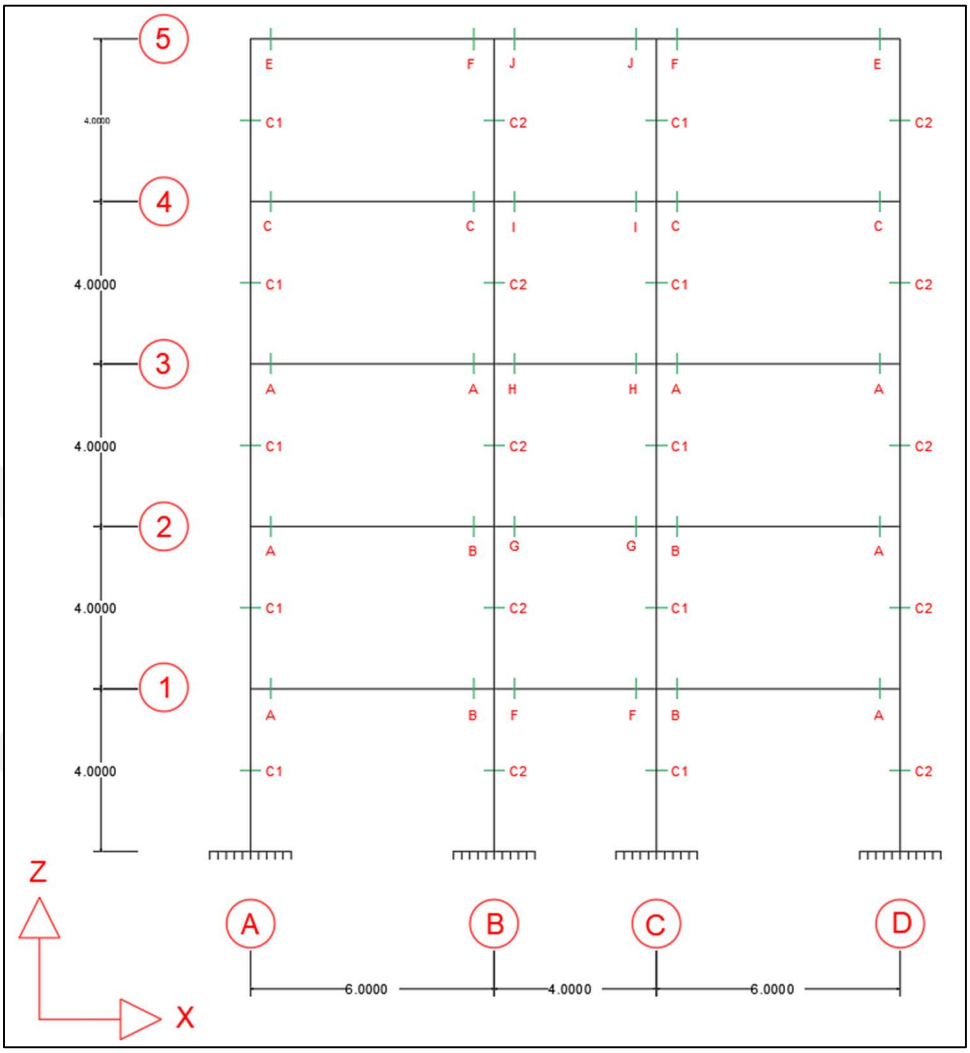

Figure 3.2: Frames' Sections and Dimensions

The dead load applied on the structure beside the structural elements self-weight are shown in table 3.1:

Table 3.1. Dead Loads on Slabs

Material type	Unit weight ($\frac{KN}{m^3}$)	Thickness (m)
Concrete Levelling	25	0.05
Concrete Pile	25	0.03
Concrete Plaster	12	0.02

The live load on the structure have been taken according to TS498 as shown in table 3.2:

Table 3.2. Live Load on Slabs

Load type	Magnitude ($\frac{KN}{m^2}$)	Reduction Factor	Magnitude ($\frac{KN}{m^2}$)
Live Load	2	0.88	1.76

In figure 3.3 and 3.4 shows dead and live load respectively coming from slabs.

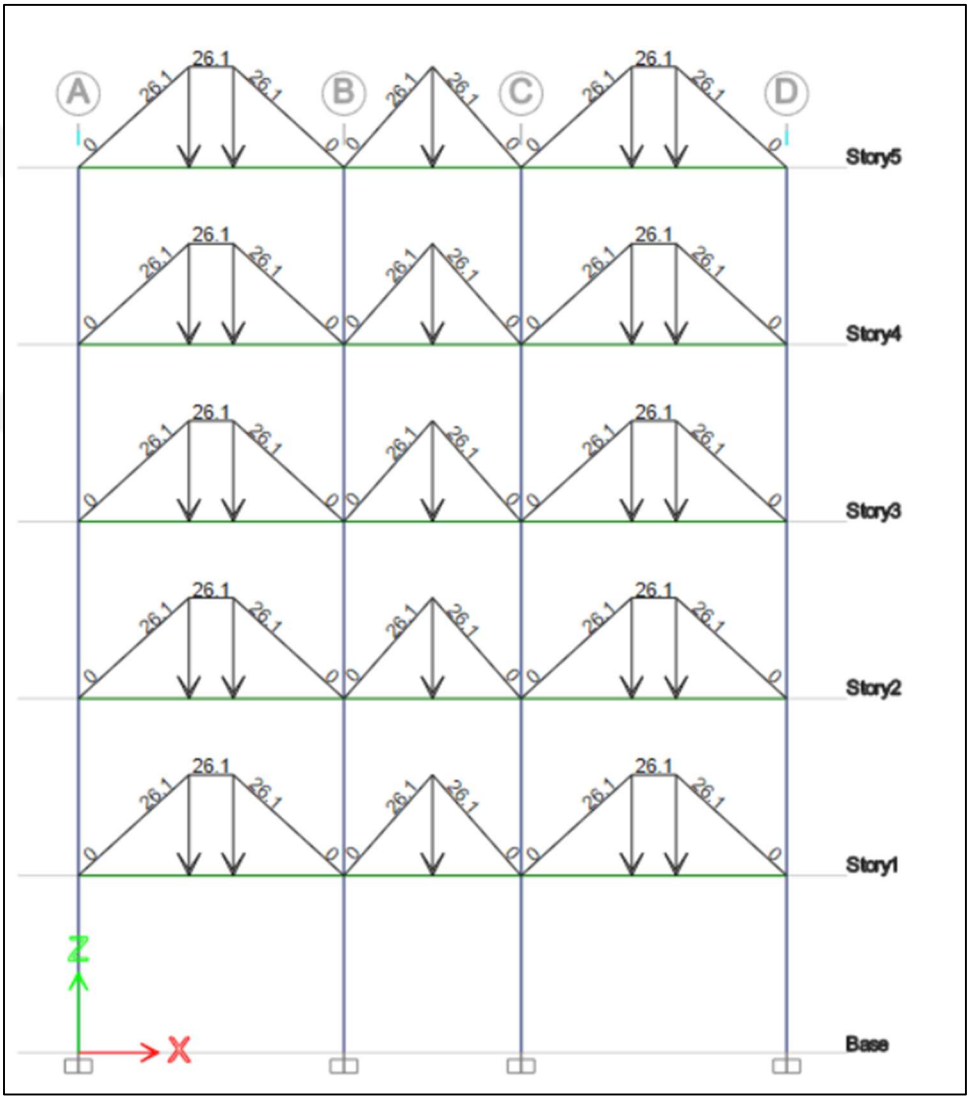

Figure 3.3: Applied dead load from slabs

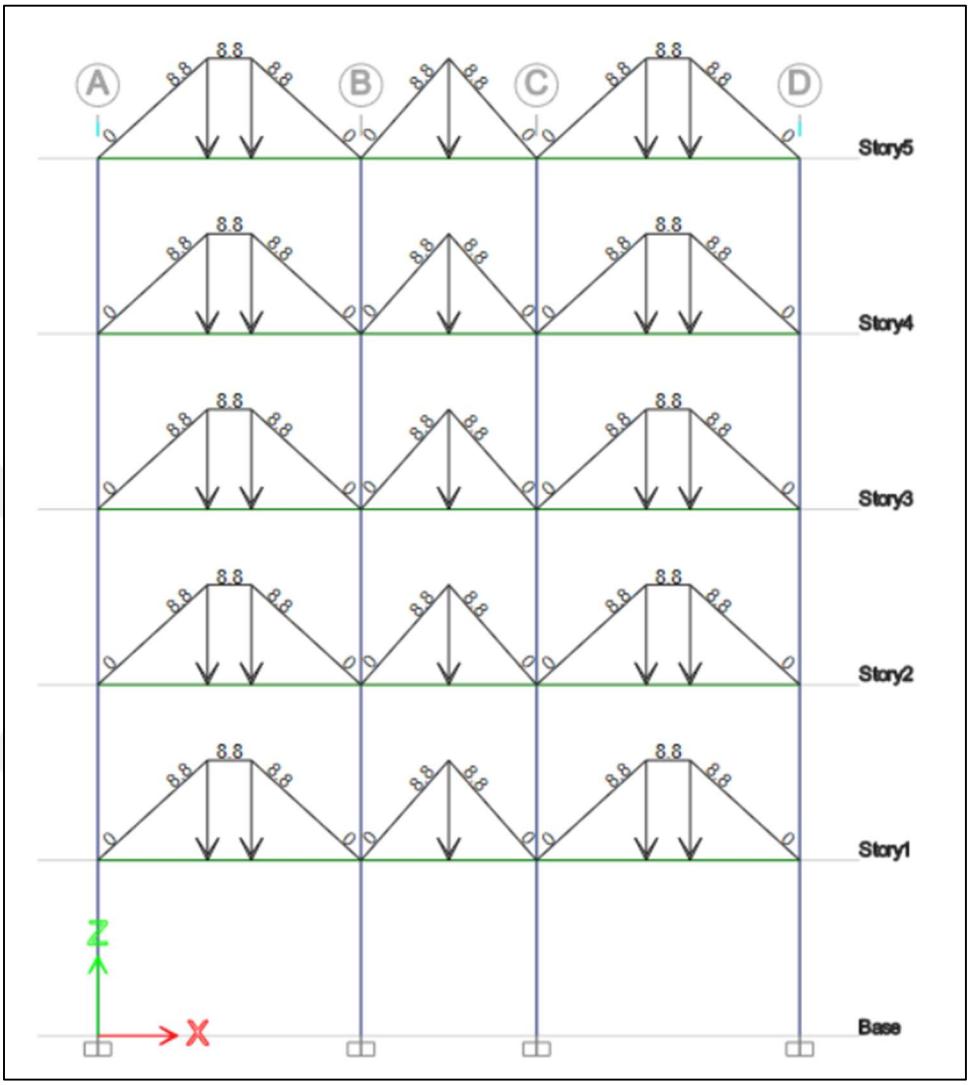

Figure 3.4: Applied dead loads from slabs

The seismic parameters of the taken location have been taken from AFAD map as shown in table 3.3:

Table 3.3. Soil and Seismic Properties

Soil Type	S_s	S_1	S_{DS}	S_{D1}
ZD	1.165	0.318	1.205	0.630

The seismic design parameters have been taken in according to TBDY2018 as in table 3.4:

Table 3.4. Seismic Design Parameters

Building usage class (BKS)	Building Importance Factor (I)	Earthquake Design Class (DTS)	Building Height Class (BYS)	Structure Behavior Factor (R)	Excess Resistance Factor (D)
3	1	1a	5	8	3

The mass source of the structure has been taken as stated in TBDY2018 table 4.3 as shown in figure 3.5

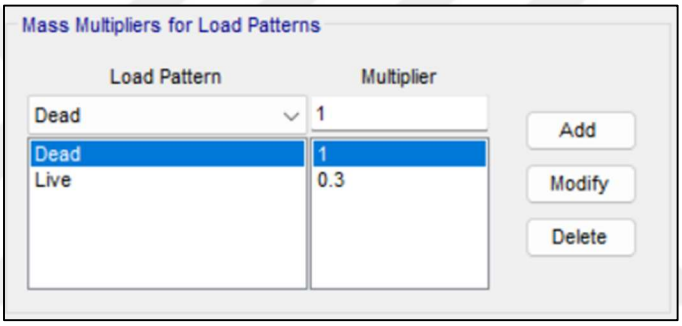

Figure 3.5: Mass source

The design load combination that has been used as:

$$1.4\,G + 1.6\,Q \tag{3.1}$$

$$G + Q + 0.2\,S + E_d^{(H)} + 0.3\,E_d^{(Z)} \tag{3.2}$$

$$0.9\,G + H + E_d^{(H)} - 0.3\,E_d^{(Z)} \tag{3.3}$$

Where

$$E_d^{(H)} = \pm E_d^{(x)} \pm 0.3\,E_d^{(y)} \tag{3.4}$$

$$E_d^{(H)} = \pm 0.3\,E_d^{(x)} \pm E_d^{(y)} \tag{3.5}$$

$$E_d^{(Z)} \approx \pm \frac{2}{3}\,S_{DS}\,G \tag{3.6}$$

The forces on the members of the dominant load combination is shown in figure from 3.6 to 3.14

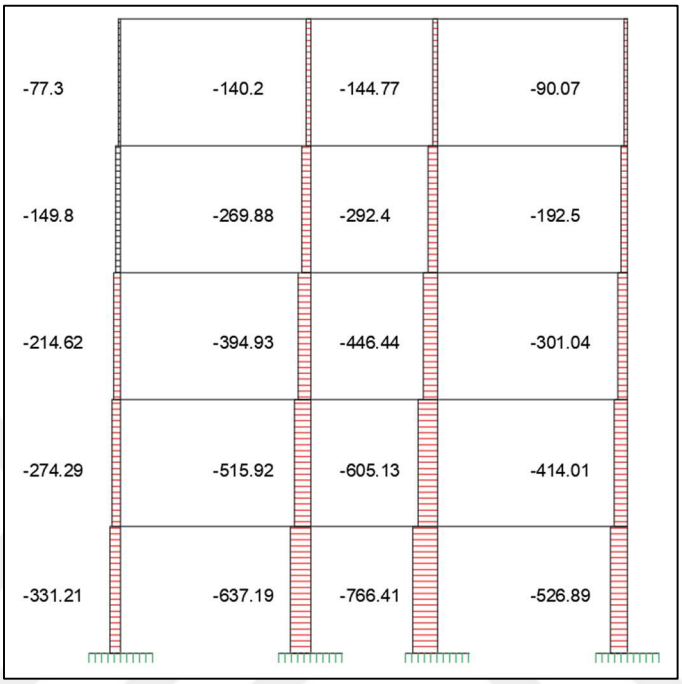

Figure 3.6: Axial forces due to forces from positive direction

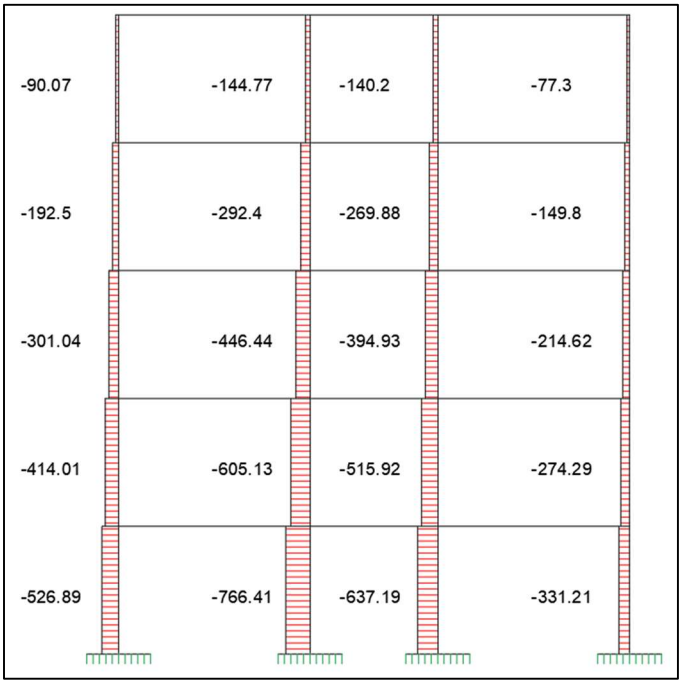

Figure 3.7: Axial forces due to forces from negative direction

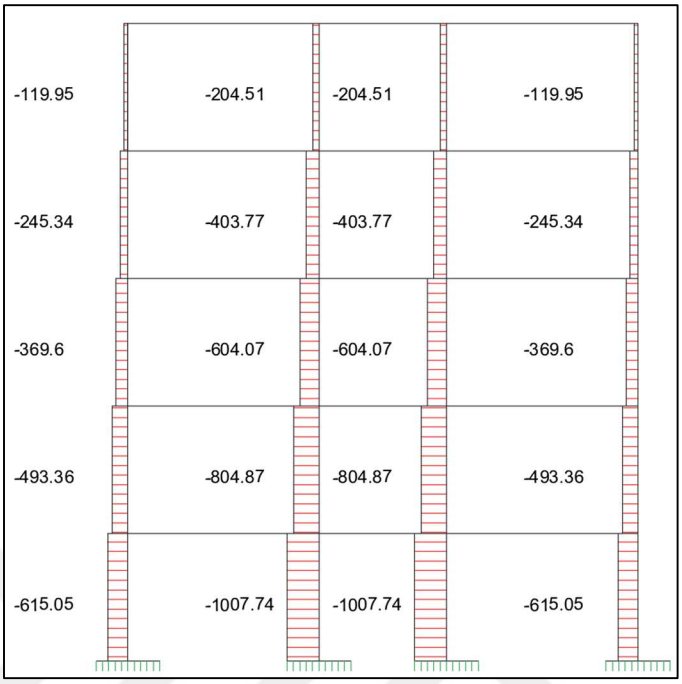

Figure 3.8: Maximum axial forces from all load combination

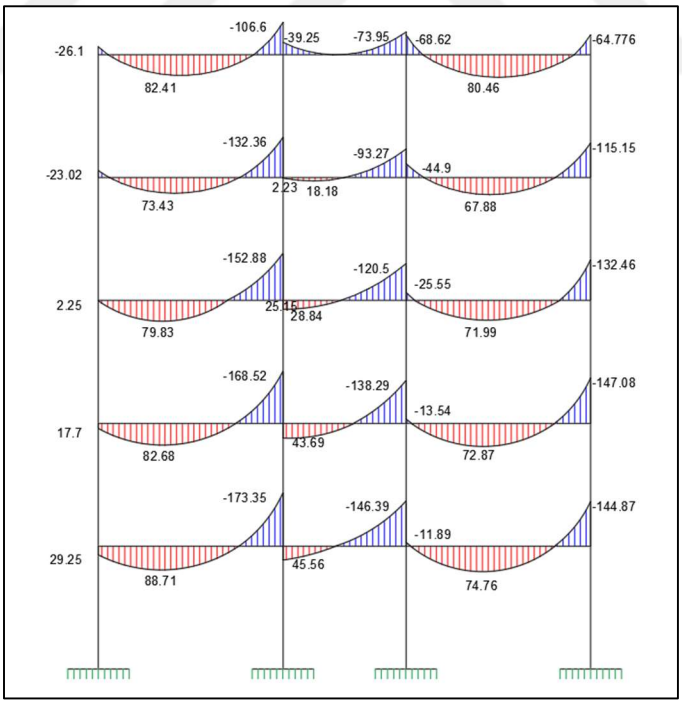

Figure 3.9: Beam moment due to forces from positive direction

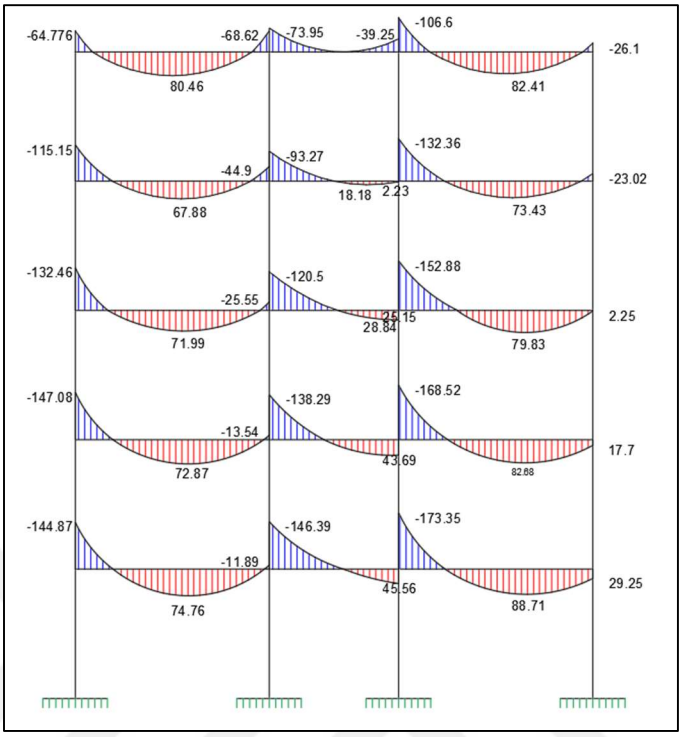

Figure 3.10: Beam moment due to forces from negative direction

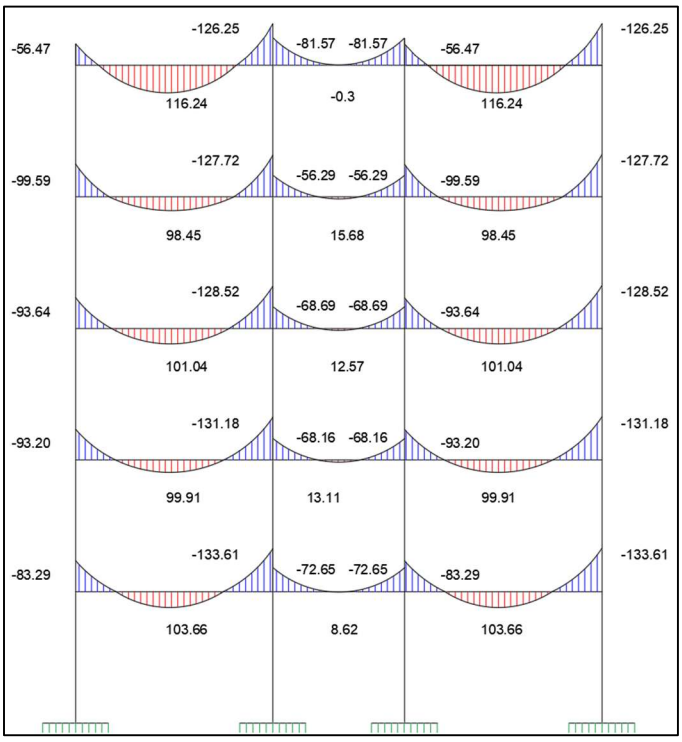

Figure 3.11: Maximum beam moments from all load combinations

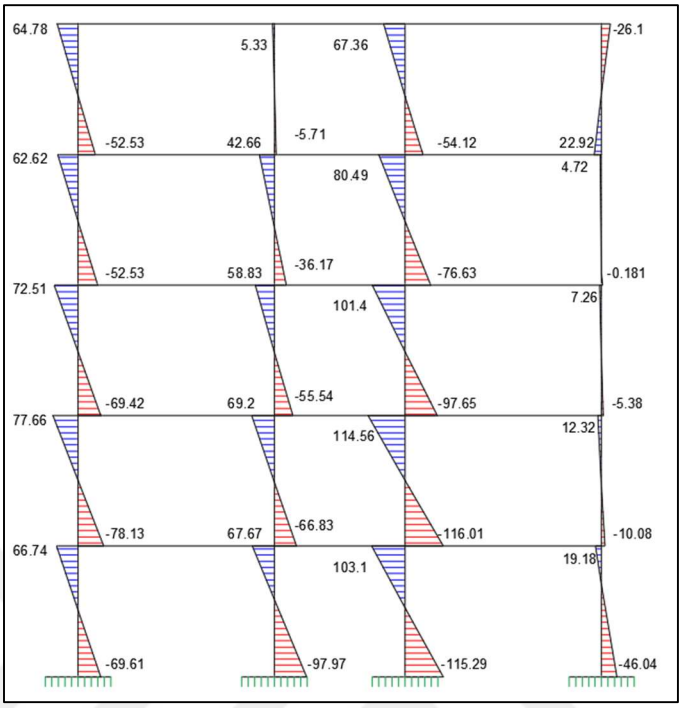

Figure 3.12: Column moment due to forces from positive direction

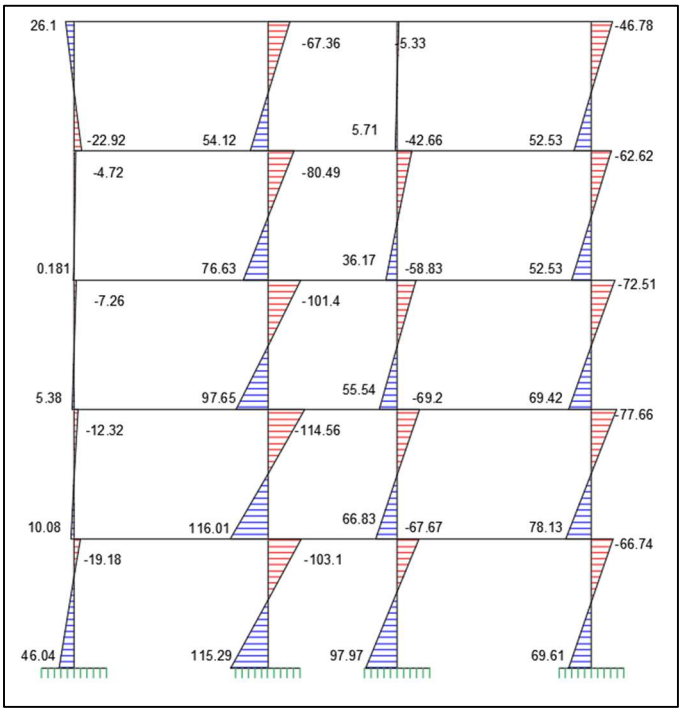

Figure 3.13: Columns moment due to forces from negative direction

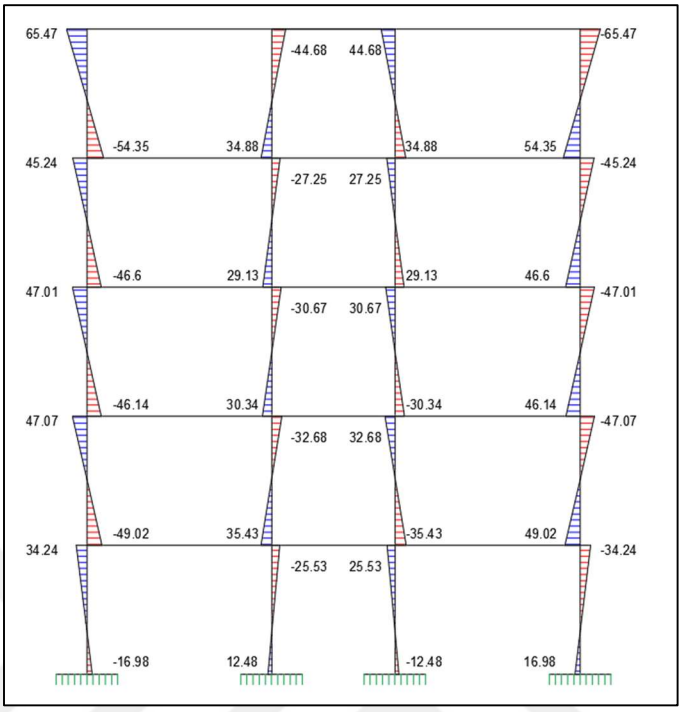

Figure 3.14: Maximum beam moments from all load combinations

According to the design load combinations, the column section has been chosen, where it can be found at the appendix section.

The reinforced concrete columns total moment capacity of the columns connected to each column-beam joint must be at least 20% greater than the total moment capacity of the beams at their sections adjoining the column faces and it can be demonstrated in figure 3.15.:

$$(M_{ra} + M_{rü}) \geq 1.2\,(M_{ri} + M_{rj}) \qquad (3.7)$$

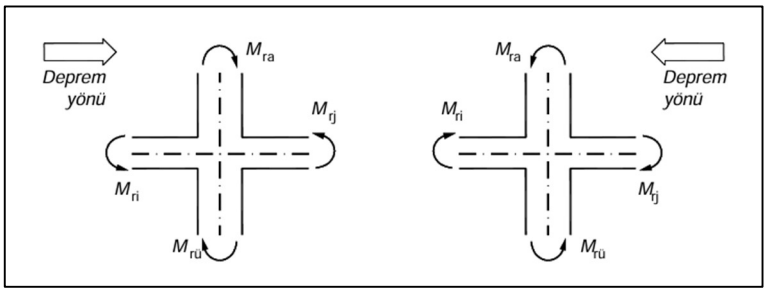

Figure 3.15: Strong column - weak beam moment capacities

The material properties used in the design used can be shown in figure 3.5:

Table 3.5. Used Materials Properties

Material Type	Grade	Modulus of Elasticity (E) Mpa
Concrete	C 25	30000
Steel	S 420	420000

The sections' details can be found in the appendix.

The non-linear material properties of the column and beam section has been taken as shown in table 3.6:

Table 3.6. Concrete Sections' Properties for Mander Calculations

Properties	C1, C2	A	B	C	D	E	F	G	H	I	J
Number of Longitudinal Reinforcement Bars	10	8	9	6	5	4	9	8	6	5	4
Number of Stirrups Reinforcement Bars in X Direction	2	2	2	2	2	2	2	2	2	2	2
Number of Stirrups Reinforcement Bars in Y Direction	2	2	2	2	2	2	2	2	2	2	2
Diameter of Stirrups Reinforcement Bars (mm)	10	10	10	10	10	10	10	10	10	10	10
Diameter of Longitudinal Reinforcement Bars (mm)	18	18	18	18	18	18	18	18	18	18	18
Clear Concrete Cover (mm)	30	30	30	30	30	30	30	30	30	30	30
Spacing Between Longitudinal Reinforcement Bars in X Direction (mm)	116.3	102	102	204	204	204	102	102	204	204	204
Spacing Between Longitudinal Reinforcement Bars in Y Direction (mm)	210	322	322	322	322	322	322	322	322	322	322
Spacing Between Transversal Reinforcement Along X Member (mm)	170	62	50.57	102	142	222	50.57	62	102	142	222
Section Width (mm)	300	300	300	300	300	300	300	300	300	300	300
Section Height (mm)	500	400	400	400	400	400	400	400	400	400	400
Unconfined Concrete Maximum Strain	0.002	0.002	0.002	0.002	0.002	0.002	0.002	0.002	0.002	0.002	0.002

Confined Concrete Strength	38.9	38.53	38.65	38.15	37.78	36.93	38.65	38.53	38.15	37.78	36.93

The Steel non-linearity parameters have been taken as shown in table 3.7:

Table 3.7. Steel Non-linear Properties

Type	$f_{sy}\ (MPa)$	ε_{sy}	ε_{sh}	ε_{su}	f_{su}/f_{sy}
S420	420	0.0021	0.008	0.08	1.15

Figures between 3.16 to 3.22 demonstrate the stress – strain curve variation between confined and unconfined reinforced concrete sections used.

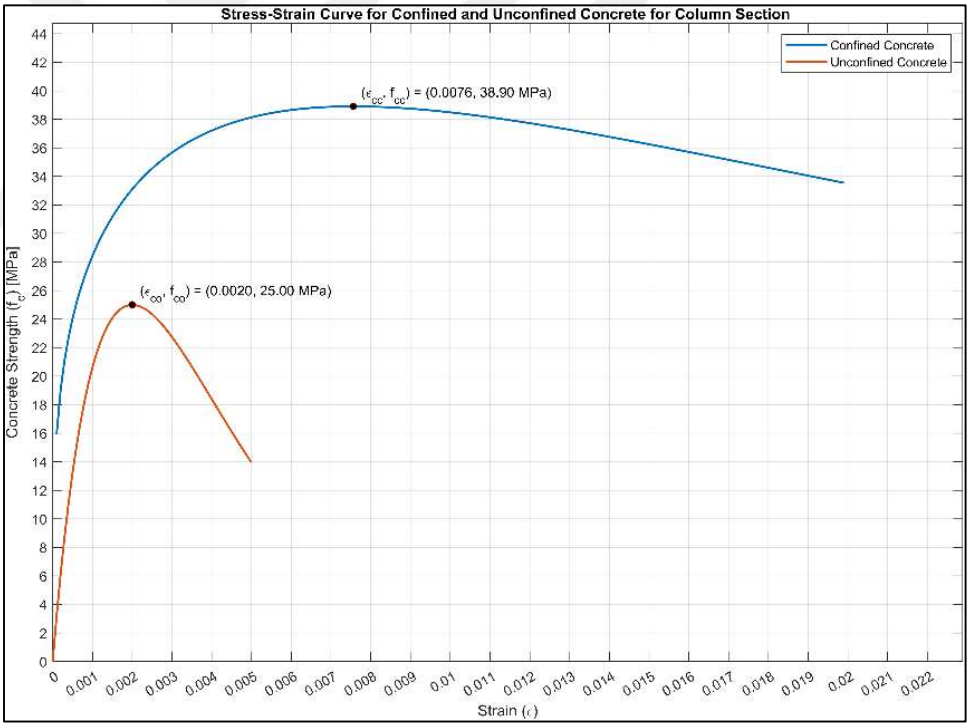

Figure 3.16: Confined and Unconfined Strength of Columns' Sections

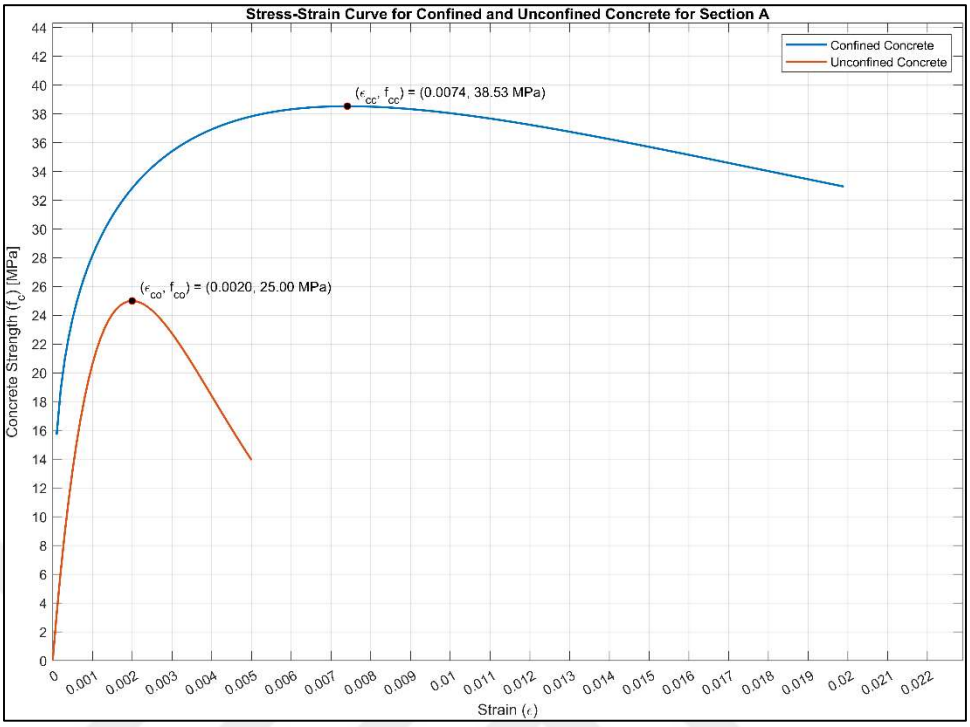

Figure 3.17: Confined and Unconfined Strength of A Sections

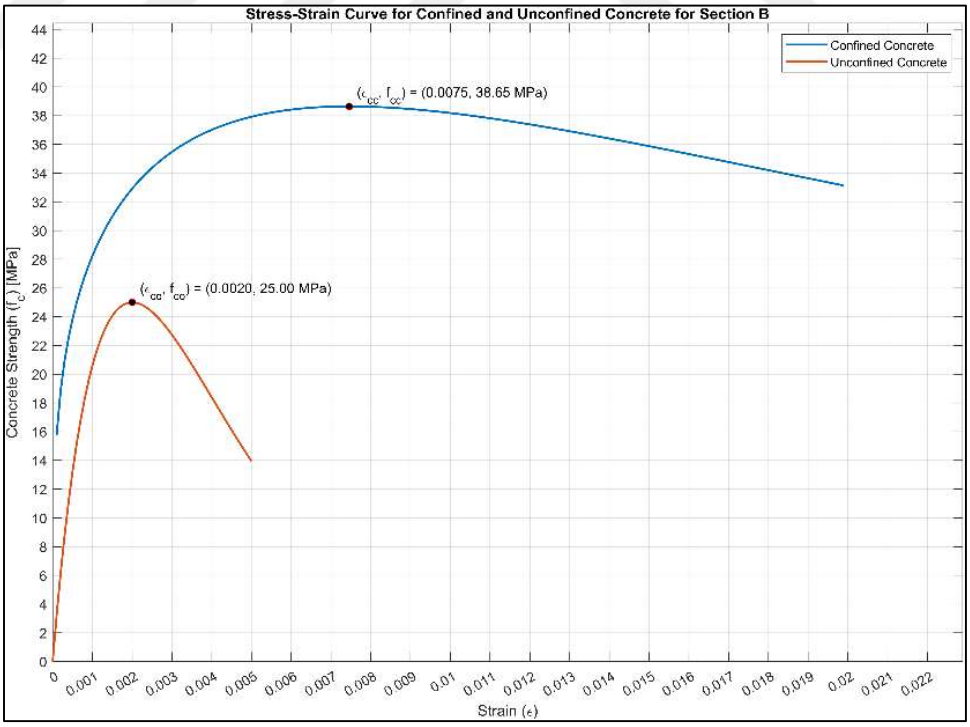

Figure 3.18: Confined and Unconfined Strength of B Sections

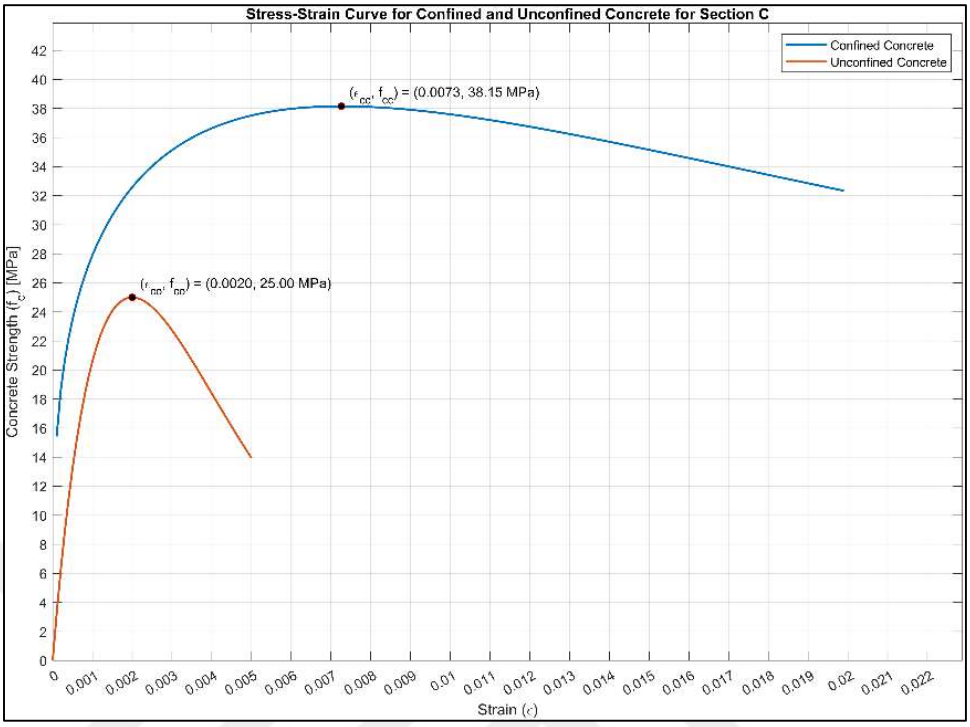

Figure 3.19: Confined and Unconfined Strength of C Sections

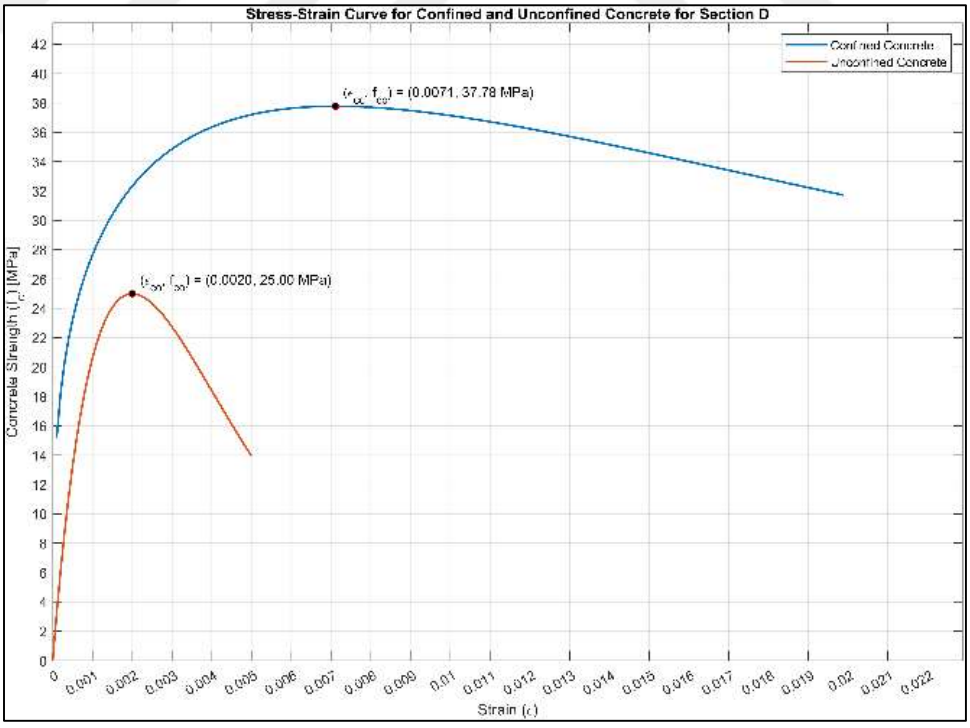

Figure 3.20: Confined and Unconfined Strength of D Sections

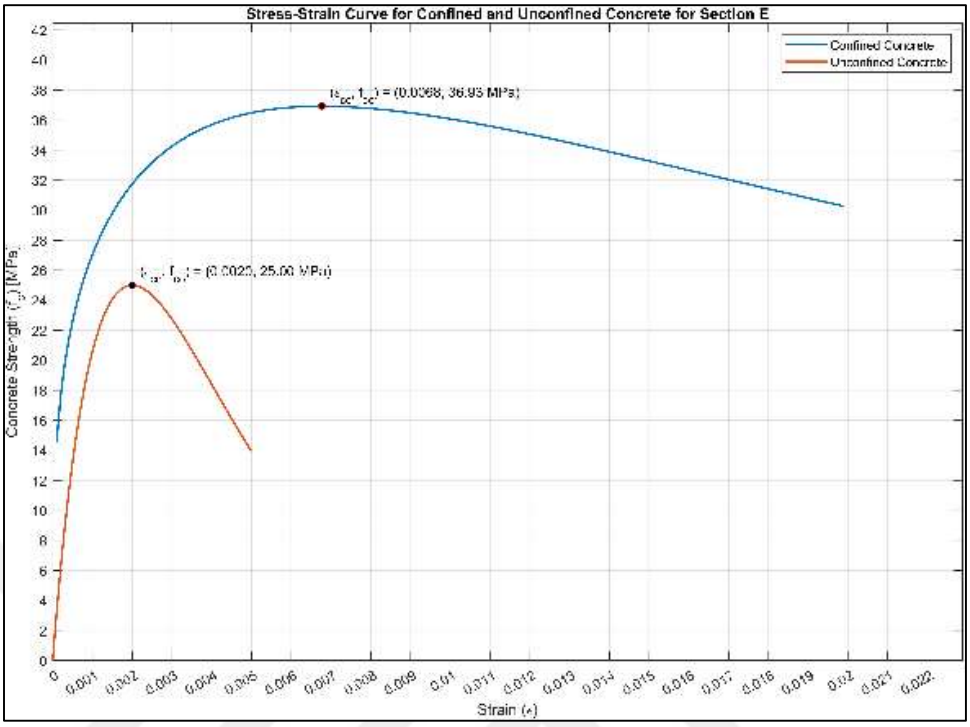

Figure 3.21: Confined and Unconfined Strength of E Sections

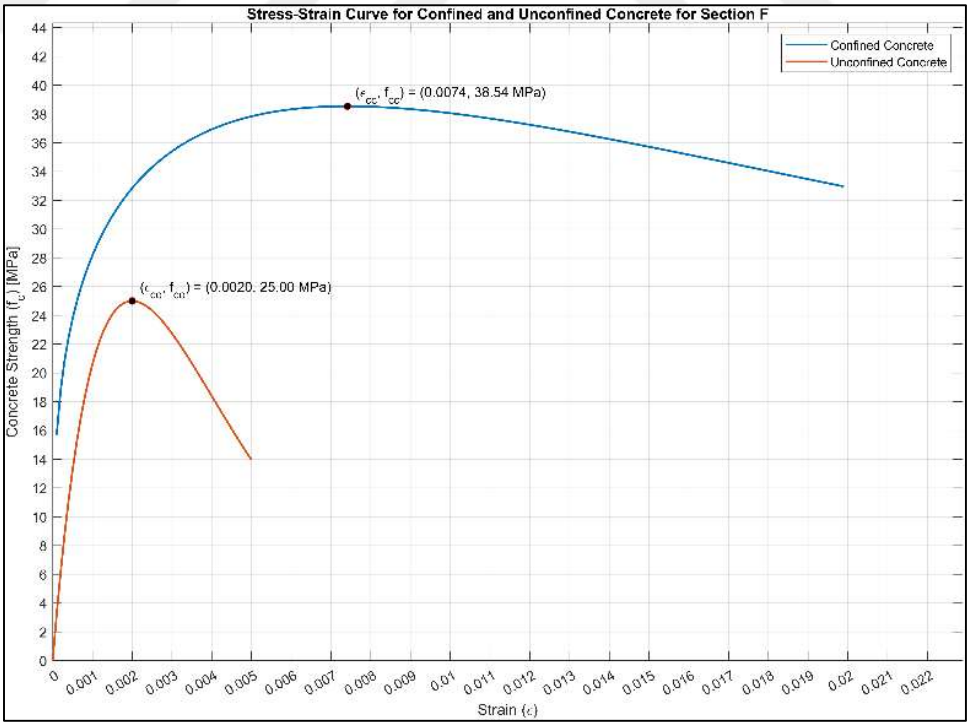

Figure 3.22: Confined and Unconfined Strength of F Sections

At each end on each member of the structure, non-linear relationship of moment-curvature has been found. Figure 3.23 to 3.26 shows strongest and weakest beam and column section

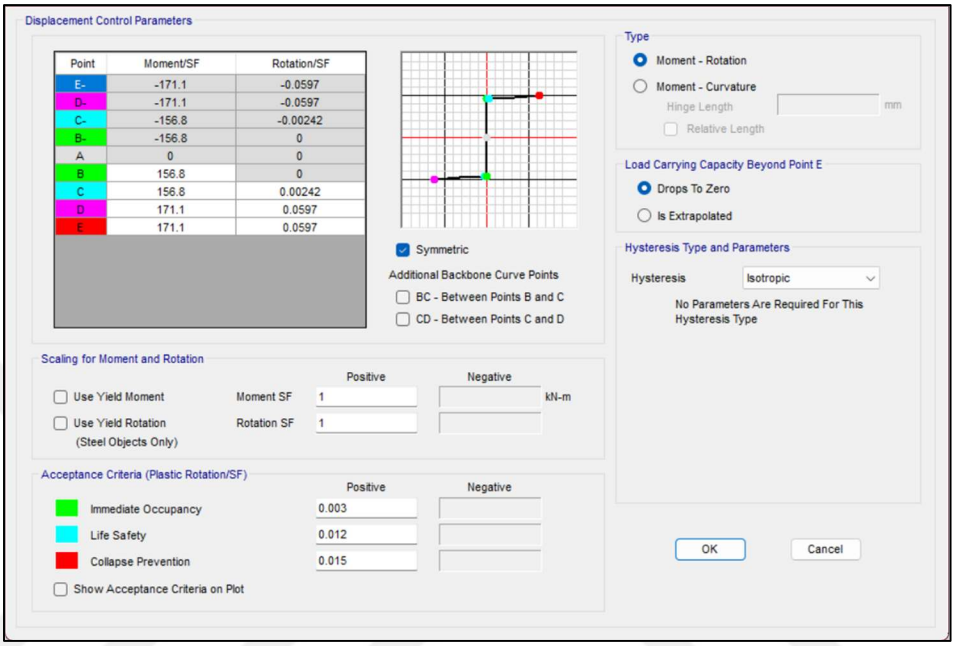

Figure 3.23: Weakest Column Section

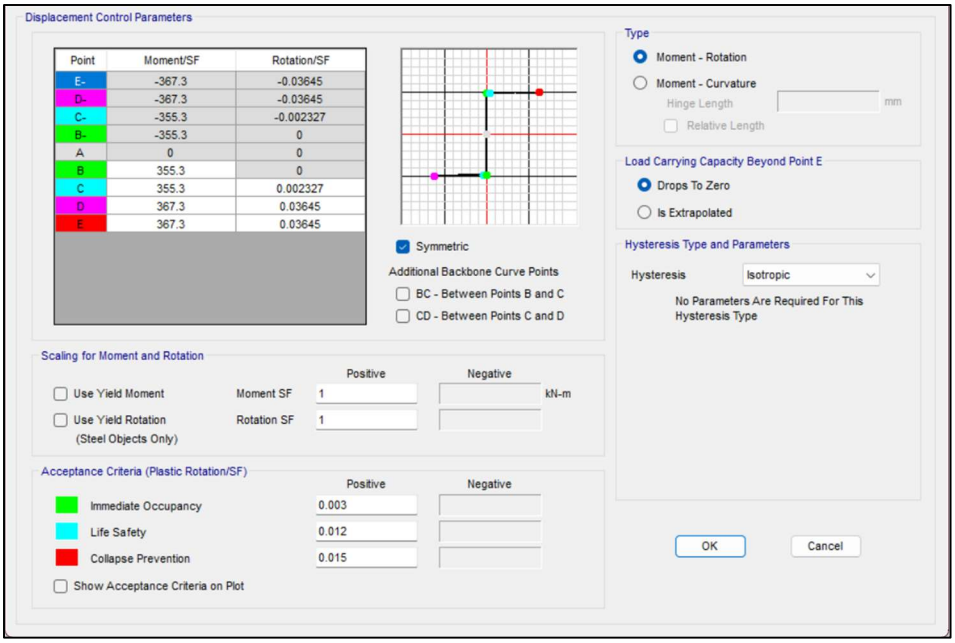

Figure 3.24: Strongest Column Section

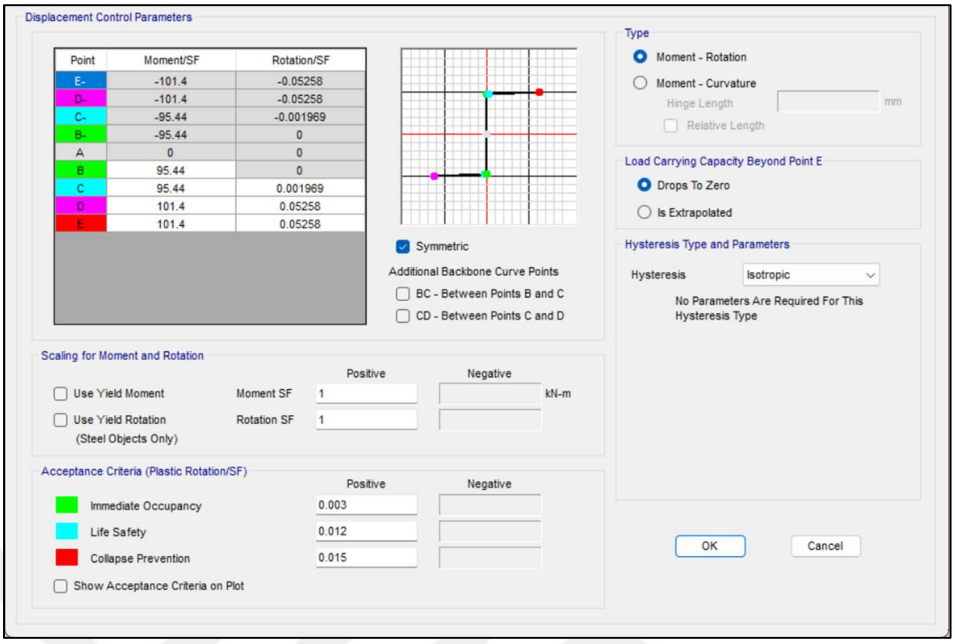

Figure 3.25: Weakest Beam Section

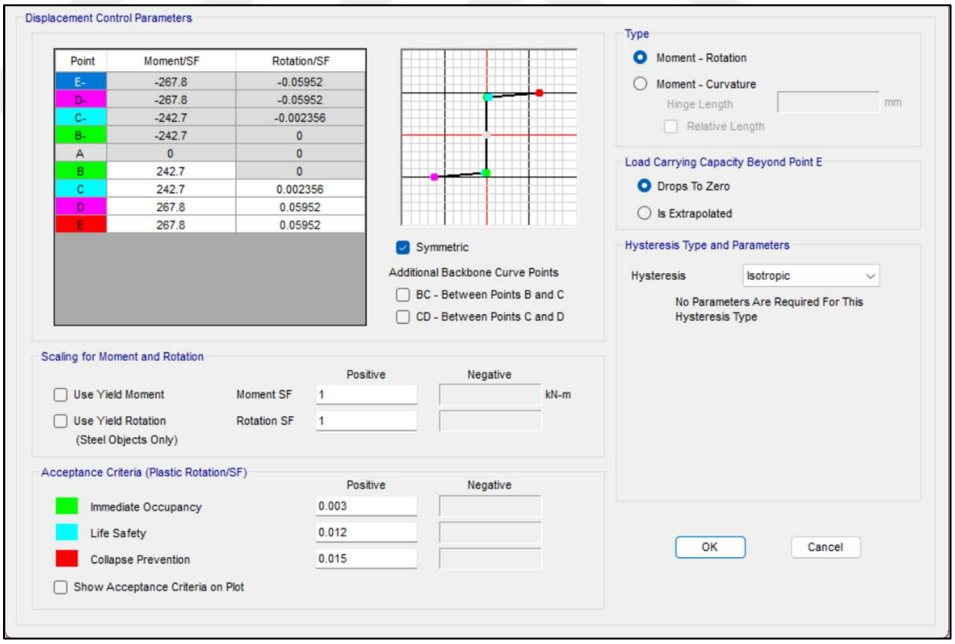

Figure 3.26: Strongest Beam Section

The mass matrix of the structure has been found as shown table 3.8:

Table 3.8. Lumped Mass of Structure

Story	Mass (Tons)
5	38.62385321
4	41.68195719
3	41.68195719
2	41.68195719
1	44.74006116

3.2. Analysis

The lateral force distribution has been done according to 4 cases:

In case 1 one the lateral force distribution has been done according to story absolute elevation from ground and the mass of it as and it can be shown in table 3.9:

Table 3.9. Lateral Force Distribution According to Equivalent Seismic Force Method

Equivalent Modal Lateral Forces					
R	8		T_A	0.104564315	
D	3		T_B	0.522821577	
I	1		S_{ae}	0.73179231	
$SD1$	0.63		S_{ar}	0.091474039	
SDS	1.205		Vtx	187.0186723	
$T1$	0.8609		Vt,min	98.5449	
mT	208.4097859		FNX	7.013200212	$V_{tx} > V_{t,min}$
Height (m)		Mass of Story (ton)		$H_i \, . m_i$	F_d (KN)
H5	20	m1	38.62385321	772.4770642	63.72233248
H4	16	m2	41.68195719	666.911315	48.9593332
H3	12	m3	41.68195719	500.1834862	36.7194999
H2	8	m4	41.68195719	333.4556575	24.4796666
H1	4	m5	44.74006116	178.9602446	13.13784014
SUMMTION				2451.987768	187.0186723

For case 2 the lateral force distribution has been done according to first mode and it can be shown in table 3.10:

Table 3.10. Lateral Force Distribution According to First Mode

Story	First Mode Shape	Lateral Force	Force
5	1	63.72233248	56.08548134
4	0.904932735	48.9593332	50.75358805
3	0.730044843	36.7194999	40.94491643
2	0.488789238	24.4796666	27.41397967
1	0.210762332	13.13784014	11.82070683
Sum	3.334529148	187.0186723	187.0186723

In case 3 the lateral force distribution is done according to modal superposition method has been used in taken into consideration only first mode as shown in table 3.11.

Table 3.11. Lateral Force Distribution According to Single Moal Participation

Step	Distribution Mode 1	mode shapes	Participation Factor mode 1
		1.st	
0	47.33112179	1	1.365761303
	46.22273104	0.904932735	
	37.28969581	0.730044843	
	24.96668822	0.488789238	
	11.55528784	0.210762332	
1	43.92782939	1	1.395582306
	43.22174317	0.911737944	
	35.45735817	0.747952684	
	24.58721917	0.518653321	
	11.52875405	0.226569609	
36	42.29415995	1	1.159864555
	42.4694137	0.930472103	
	30.24574482	0.662660944	
	15.55383509	0.340772532	
	0.210264259	0.004291845	

In case 4 the lateral force distribution has been done according to modal superposition method has been used in taken into consideration only first two mode which can be briefly demonstrated in table 3.12.

Table 3.12. Lateral Force Distribution According to Two Modal Participation

Step	Distribution Mode 1	Distribution Mode 2	mode shapes		Participation Factor mode 1	Participation Factor mode 2
			1.st	2.nd		
0	47.3311	-18.1028	1.0000	1.0000	1.3658	-0.5224
	46.2227	-4.8746	0.9049	0.2495		
	37.2897	12.9422	0.7300	-0.6625		
	24.9667	20.7075	0.4888	-1.0600		
	11.5553	13.8106	0.2108	-0.6586		
1	48.3646	-13.8475	1.0000	1.0000	1.3956	-0.3996
	47.5872	-4.0652	0.9117	0.2720		
	39.0386	9.3900	0.7480	-0.6284		
	27.0706	15.7168	0.5187	-1.0517		
	12.6932	10.4784	0.2266	-0.6533		
29	48.3646	-14.6360	1.0000	1.0000	1.3956	-0.4223
	50.7510	-6.0596	0.9724	0.3836		
	46.4222	14.4415	0.8894	-0.9143		
	25.0770	15.4565	0.4805	-0.9786		
	0.6409	6.8013	0.0114	-0.4012		

3.3. Results

The analysis produced five main results:

Displacement and Base Shear Force Behavior

Case 1: Exhibited the highest top roof displacement of 340 mm with a lateral load parameter of 2.873.

Case 2: Produced slightly less displacement at 335.144 mm, with a higher lateral load parameter of 2.905.

Case 3: Demonstrated a significant change in P−Δ curve behavior, showing a displacement of 306 mm and a marked increase in P to 3.810.

Case 4: Showed the smallest displacement at 210 mm with lateral load parameter of 3.692. Early hinge formation in the bottom columns of Story 2 and the top of Story 4 affected the results, leading to reduced lateral force capacity.

The comparison can be shown in figure 3.27

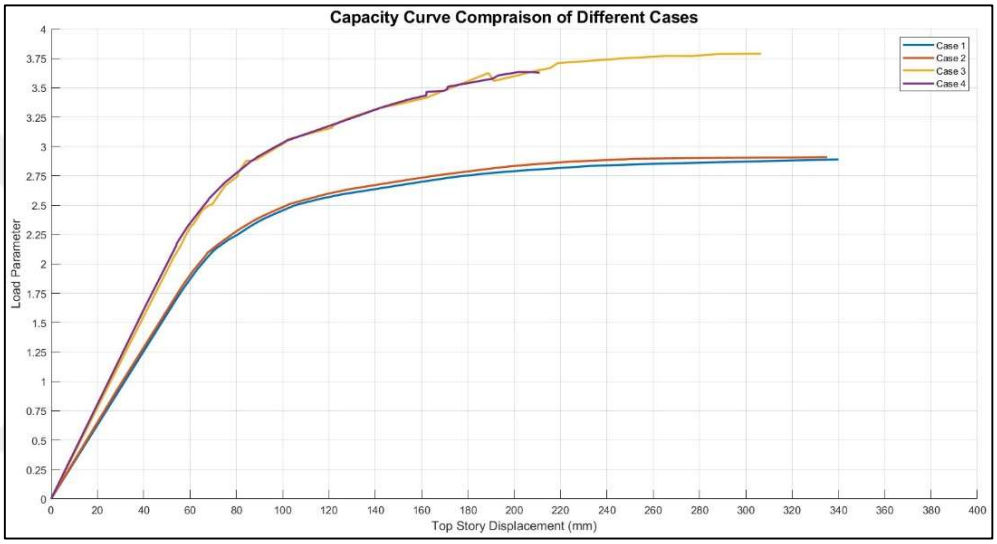

Figure 3.27: Capacity Curve Comparison of Four Cases

Natural Period and Base Shear Force Behavior

Case 1: Achieved a lateral load parameter of 2.873 before failure, with a natural period of 7.35 seconds.

Case 2: Reached a lateral load parameter of 2.905, with the natural period extending to 10.051 seconds—possibly due to a greater number of hinges compared to other cases.

Case 3: At lateral load parameter of 3.810, the natural period was 8.656 seconds.

Case 4: Displayed the lowest natural period at 5.93 seconds with a lateral load parameter of 3.692. Early hinge formation in columns led to failure before significant structural stiffness reduction could occur.

The comparison can be shown in figure 3.28

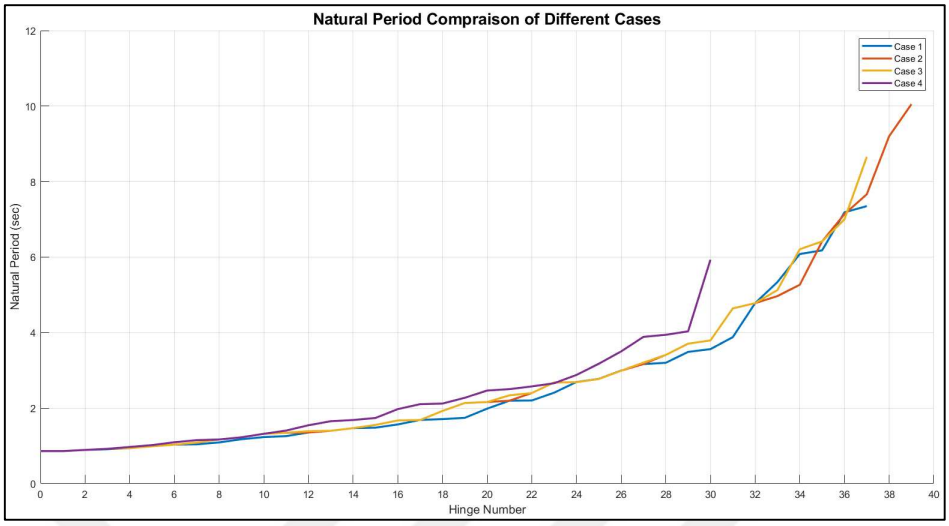

Figure 3.28: Natural Period Change Comparison of Four Cases

Stability Load Parameter

Initial Value: All cases started with a stability load parameter of 16.26153.

Case 1: Reached zero after 37 hinges formed.

Case 2 and Case 3: Showed similar stability load parameter reduction, with Case 2 reaching zero after 39 hinges and Case 3 after 37 hinges.

Case 4: Displayed the steepest reduction, reaching zero after only 30 hinges due to faster failure of critical nodes, resulting in an earlier mechanism state.

The comparison can be shown in figure 3.29

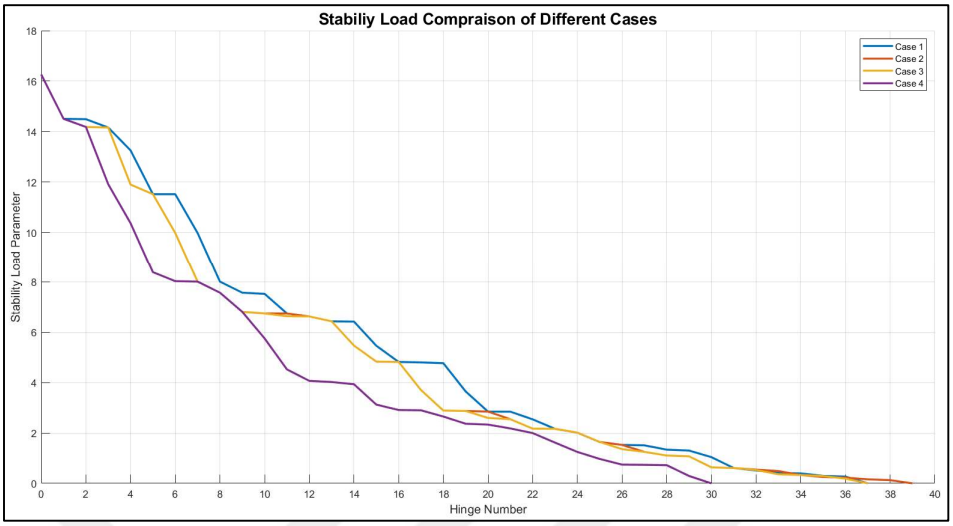

Figure 3.29: Stability Load Change of Four Cases

First Modal Participation Factor

Across all cases, the first modal participation factor initially increased, followed by a significant decrease.

Case 1: Showed the largest reduction, starting at 1.366 and ending at 1.16.

Case 2 and Case 3: Displayed similar trends, with Case 2 ending at 1.194 and Case 3 at 1.159.

Case 4: Experienced minimal reduction, starting at 1.366 and concluding at 1.365 in the final step.

The comparison can be shown in figure 3.30

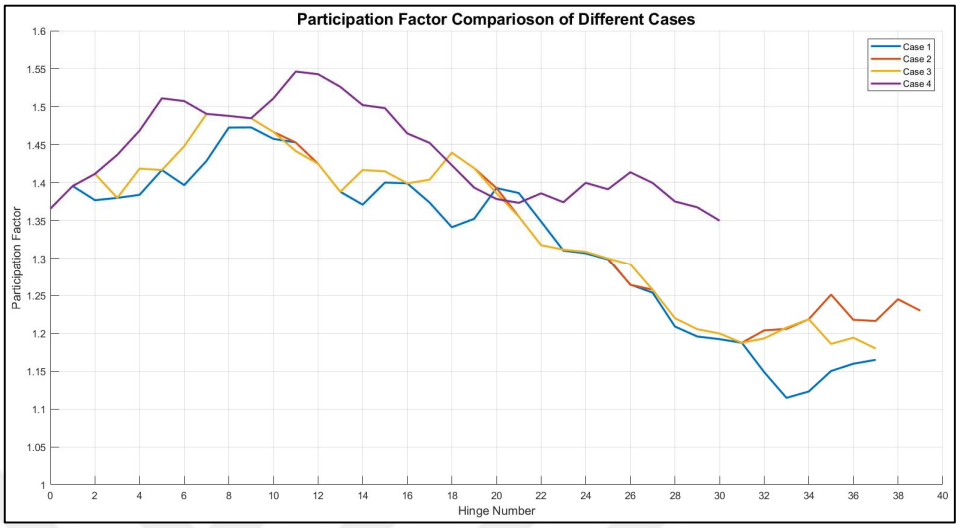

Figure 3.30: Participation Factor Change for Four Cases

Effect on Mode Shape Sequence

After each hinge formation, mode shapes shifted from their original positions.

Case 1: Showed the most significant shift in one direction between earlier and later mode shapes.

Case 2 and Case 3: Displayed similar results, where Stories 1, 2, and 3 shifted in one direction.

Case 4: Exhibited different behavior. Stories 1 and 2 experienced less shift compared to other cases, while Stories 3 and 4 displayed significant shifts in the opposite direction.

The hinge sequence of all cases can be demonstrated in figures 3.31 to 3.35

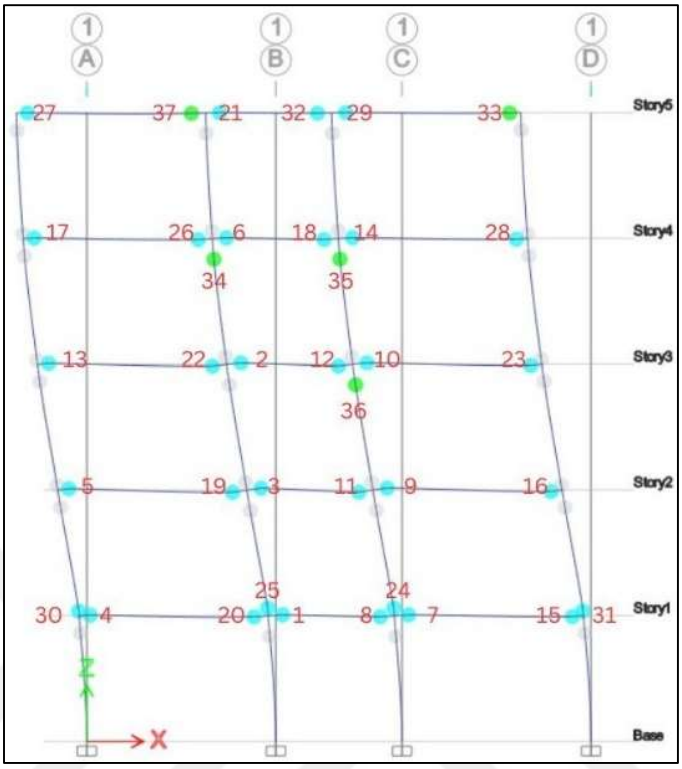

Figure 3.31: Hinge Sequence of First Case

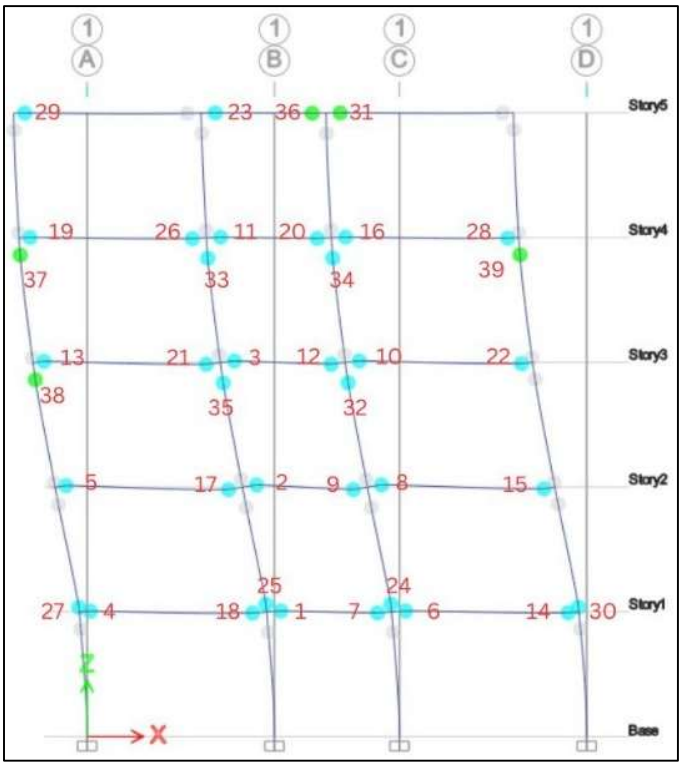

Figure 3.32: Hinge Sequence of Second Case

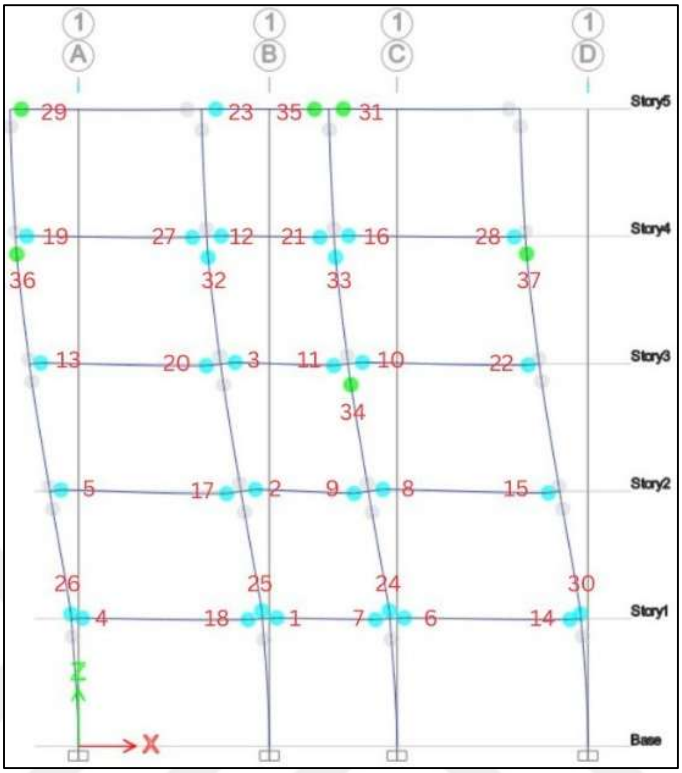

Figure 3.33: Hinge Sequence of Third Case

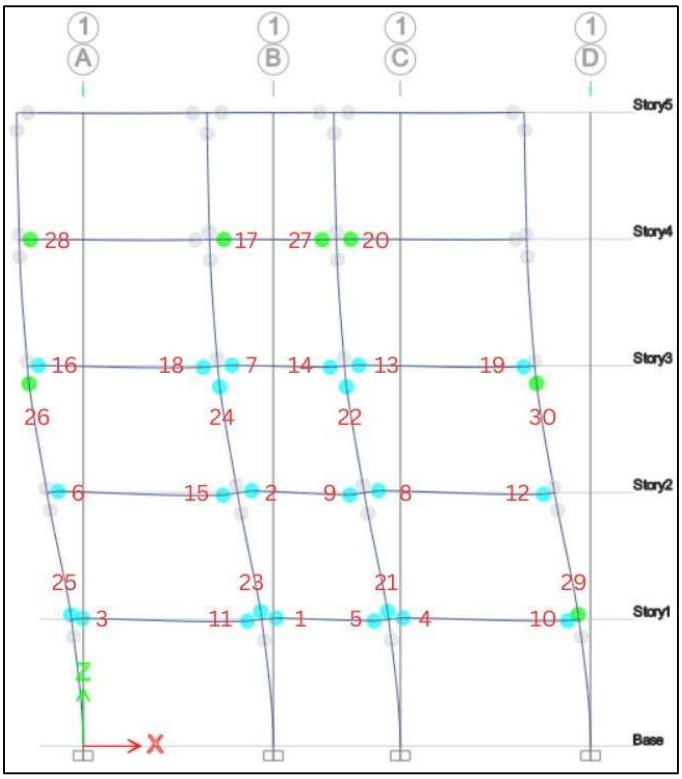

Figure 3.34: Hinge Sequence of Fourth Case

The initial structure mode shape can be shown in figure 3.35, while a comparison between initial and last mode shapes of the structure can be found in figures 3.36 to 3.39

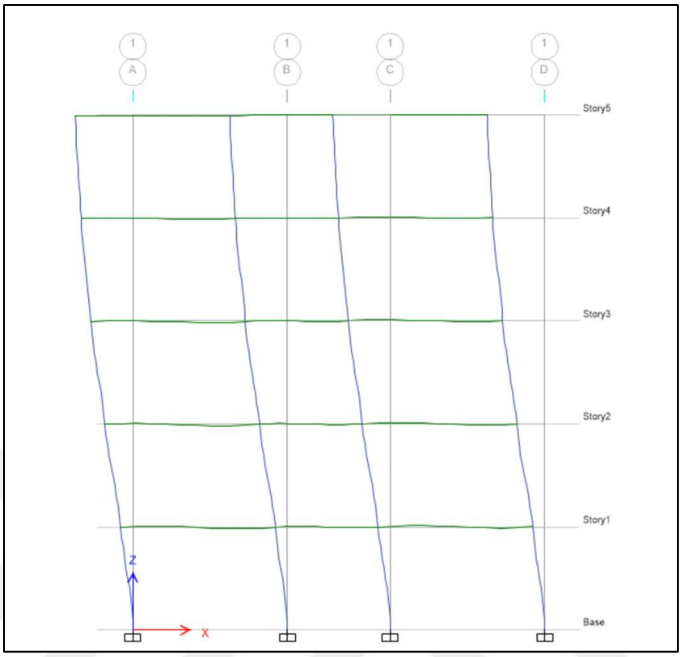

Figure 3.35: Initial structure mode shape

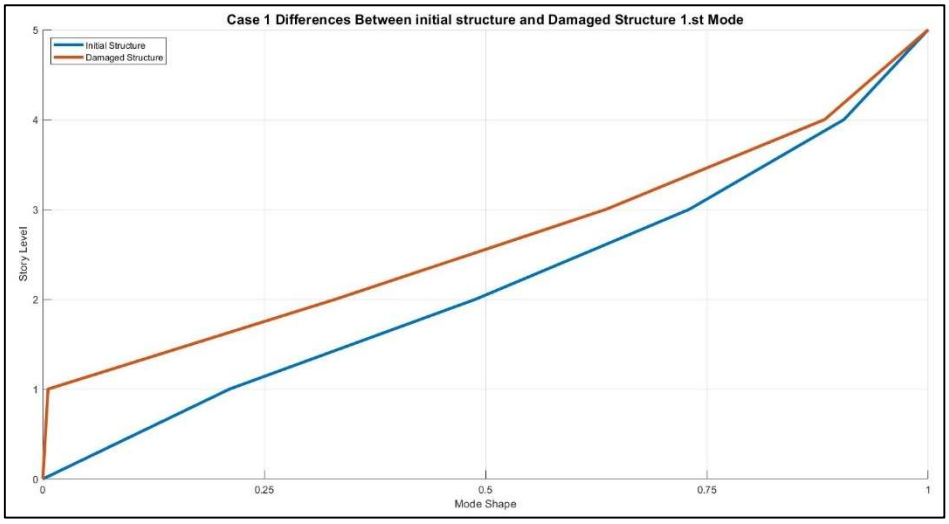

Figure 3.36: Initial and last mode shapes comparison for case 1

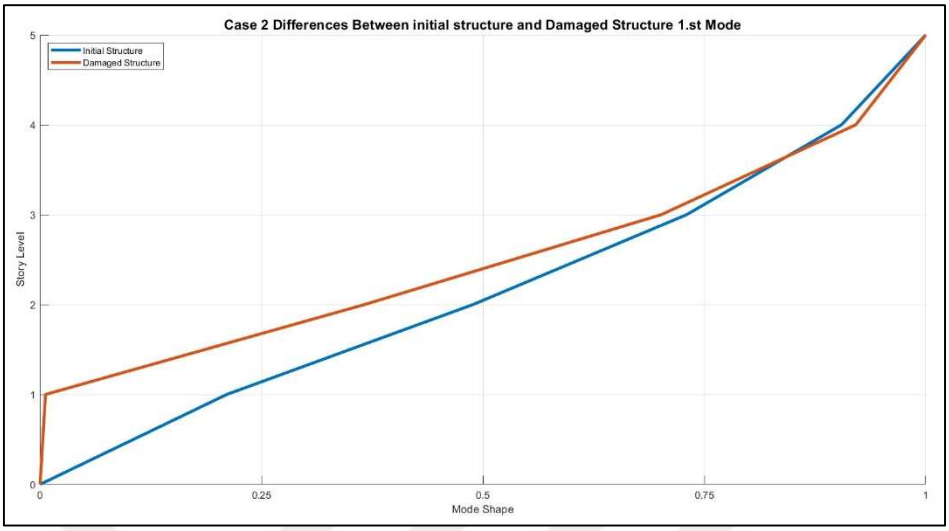

Figure 3.37: Initial and last mode shapes comparison for case 2

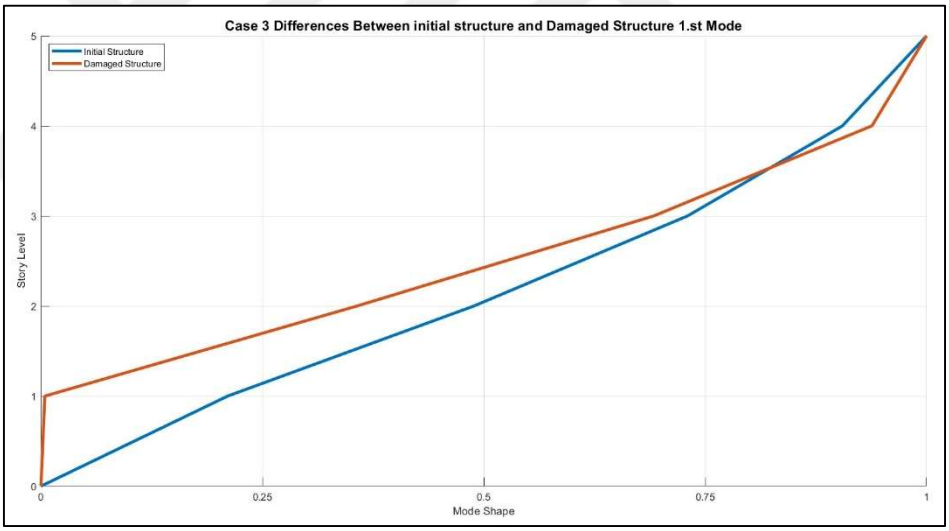

Figure 3.38: Initial and last mode shapes comparison for case 3

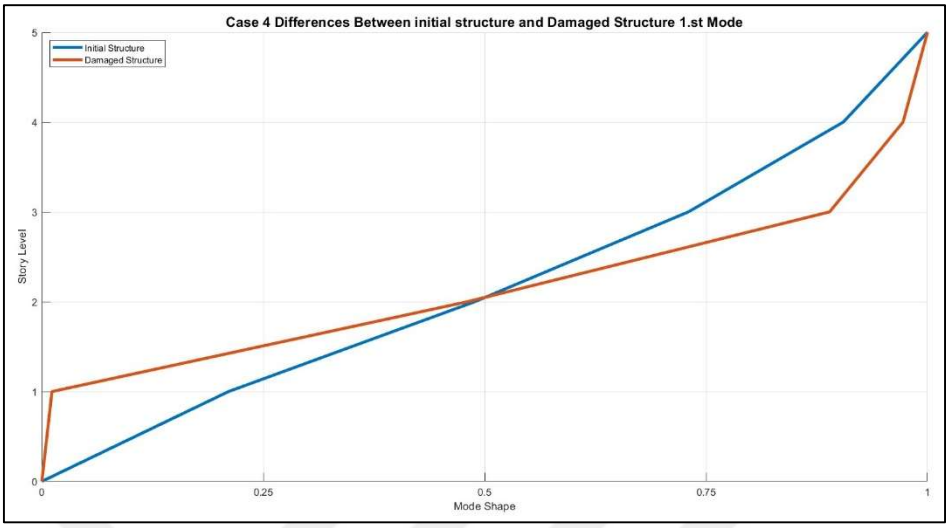

Figure 3.39: Initial and last mode shapes comparison for case 4

A comparison between all mode shapes of the structure can be found in figures 3.40 to 3.43

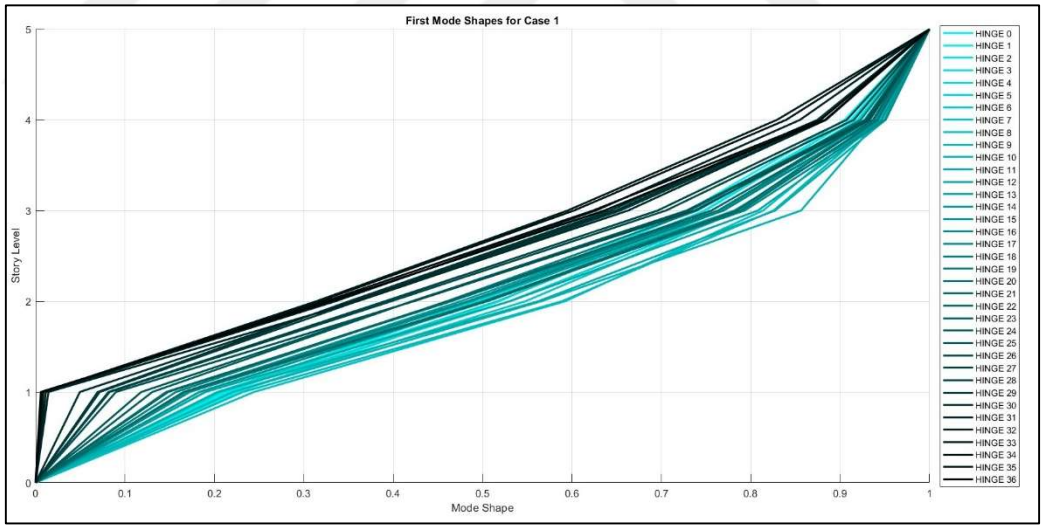

Figure 3.40: Mode Shapes at Each hinge of First Case

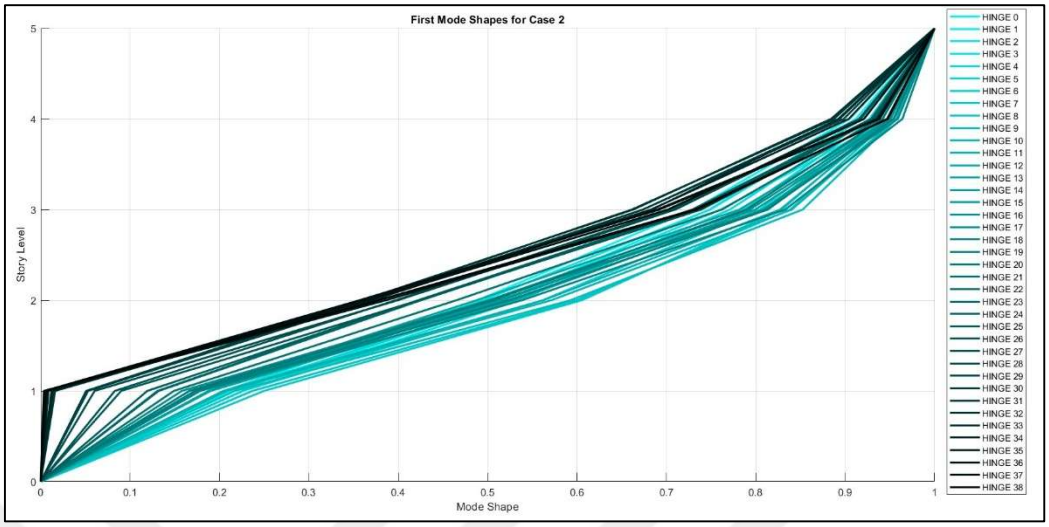

Figure 3.41: Mode Shapes at Each hinge of Second Case

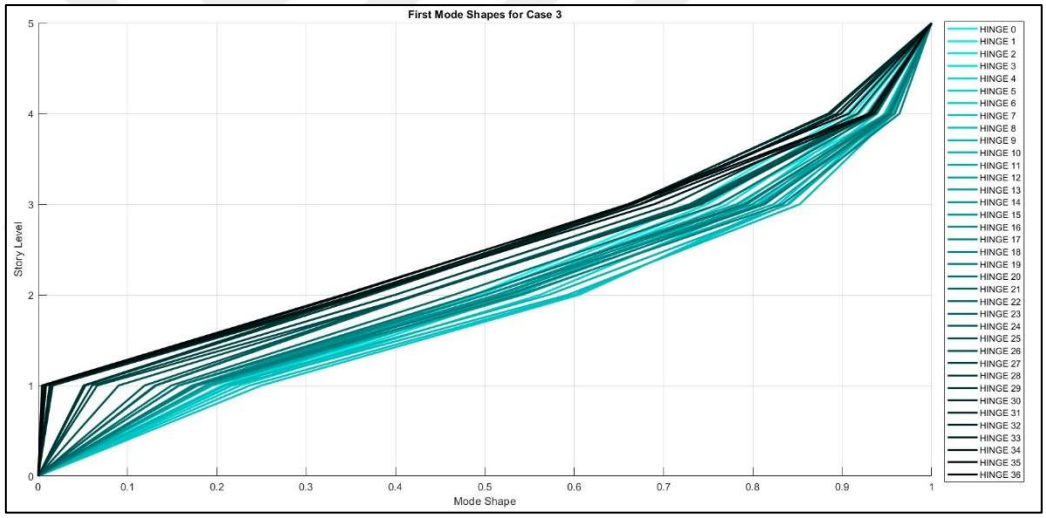

Figure 3.42: Mode Shapes at Each hinge of Third Case

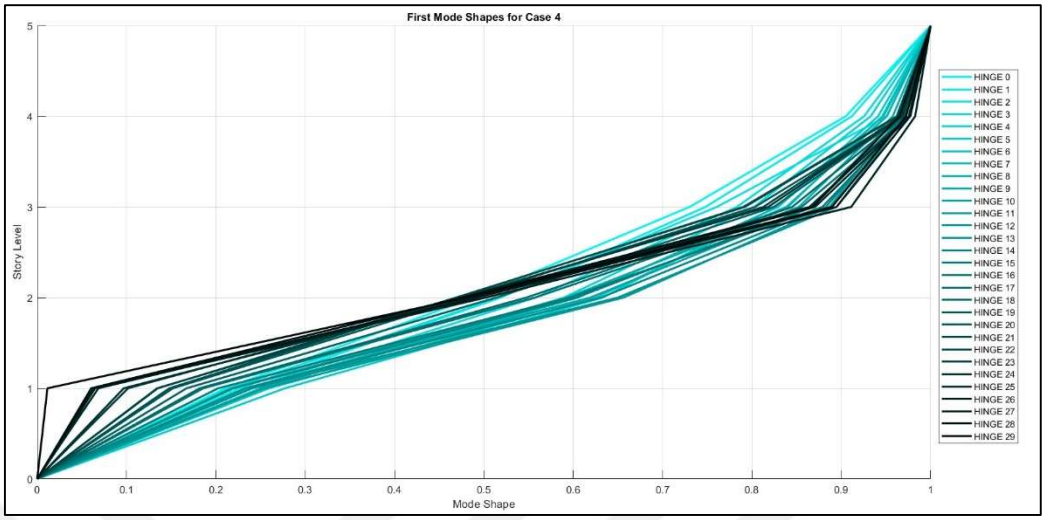

Figure 3.43: Mode Shapes at Each hinge of Fourth Case

In general case 4 shows most, realistic results compared to the other cases because it traces the real behavior of the structure. When hinge happens, the stiffness of the whole frame changes, which will lead to change in lateral forces as shown in cases 3 and 4. While in case 4 the second mode shape taken into consideration brings us a step closer to having a more realistic simulation.

4. CONCLUSION AND FUTURE IMPLEMENTATION

The primary goal of this study was to compare the pushover capacity curve and free vibration analysis parameters—fundamental period, mode shapes, modal participation factors, and load stability—derived from second-order analysis of axial loads on columns. By conducting free vibration analysis at each hinge occurrence, valuable insights were gained into the structural behavior under seismic actions. The procedure was applied to four distinct lateral load distribution cases:

Case 1: Lateral force distributed by story mass and absolute elevation.

Case 2: Based on the first mode shape.

Case 3: Based on first-mode modal contribution.

Case 4: Incorporating contributions from two modes.

The study produced five key findings:

Displacement and Base Shear Force Behavior

Case 1 exhibited the highest displacement but the lowest base shear force, while Case 2 showed marginally lower displacement and slightly higher base shear force. Case 3 resulted in a significant increase in base shear force with only a small change in displacement compared to Cases 1 and 2. Case 4, on the other hand, demonstrated the least displacement and the highest base shear force. These contrasting behaviors underscore the structural variability under different lateral loading scenarios.

Natural Period and Base Shear Force

The formation of hinges during the pushover analysis reduced rotational stiffness, leading to an increase in both the natural period and base shear force. Cases 1 and 2 showed comparable pushover curve behaviors, while Case 4 demonstrated lower natural period and base shear force values than Case 3. This variation can be attributed to the number and location of hinge formations before structural failure.

Stability Load Parameter

The stability load parameter diminished as hinges formed during the pushover analysis. The rate of decrease was influenced by hinge locations and configurations. Case 1 exhibited the least reduction, while Cases 2 and 3 showed similar moderate reductions. Case 4 experienced the most significant reduction, particularly in the early stages, making the structure more susceptible to failure due to P−Δ effects under compressive forces. This highlights the reduced safety margin against buckling, which can occur before the structure reaches its limit load.

First Modal Participation Factor

The first modal participation factor fluctuated during the pushover analysis due to hinge formations. Case 1 remained the most stable, maintaining the highest values throughout the analysis and up to collapse. Cases 2 and 3 experienced moderate fluctuations before significant reductions, whereas Case 4 exhibited the steepest reductions, particularly in the final stages.

Effect on Mode Shape Sequence

The sequence and configuration of hinge formations notably impacted the mode shape sequence. Case 1 showed the most substantial shifts in mode shapes. Cases 2 and 3 exhibited similar behaviors, with moderate shifts. In Case 4, the upper and lower stories shifted in opposite directions, emphasizing the impact of hinge formations on the dynamic behavior of the structure.

Future Implications

This study highlights the need for further exploration of seismic responses in steel frame structures, which differ significantly from concrete frames due to material properties. Future research should focus on the modal characteristics, seismic responses, and stability of steel frames under varying lateral load distributions. Such investigations will contribute to the development of optimized designs for seismic-resistant steel frame buildings.

REFERENCES:

[1] Takeda, T., Sozen, M. A., & Nielsen, N. N. (1970). Reinforced concrete response to simulated earthquakes. Journal of the Structural Division, 96(12), 2557–2573. https://doi.org/10.1061/jsdeag.0002765

[2] Kilar, V., & Fajfar, P. (1996). Simplified push-over analysis of building structures. In Proceedings of the Eleventh World Conference on Earthquake Engineering. Elsevier Science Ltd. (Paper No. 1011).

[3] Habibullah, A., & Pyle, S. (1998). Practical three dimensional nonlinear static pushover analysis. Structure Magazine, (Winter).

[4] Krawinkler, H., & Seneviratna, G. (1998). Pros and cons of a pushover analysis of seismic performance evaluation. Engineering Structures, 20(4–6), 452–464. https://doi.org/10.1016/s0141-0296(97)00092-8

[5] Mert-Tugsal, Ū., Taskin, B., & Kara, F. I. (2008). Comparison of performance evaluation concept for RC buildings considering Turkish earthquake code and the proposed empirical relation. In Proceedings of the 14th World Conference on Earthquake Engineering (pp. 1–8). Beijing, China.

[6] Abhilash, R., Biju, V., & Leslie, R. (2009, November 6-7). Effect of lateral load patterns in pushover analysis. 10th National Conference on Technological Trends (NCTT09), College of Engineering Trivandrum.

[7] Etedali, S., & Irandegani, M. A. (2015). A proposed lateral load pattern for pushover analysis of structures subjected to earthquake excitations. Journal of Vibroengineering, 17(3), 1363–1371. https://www.jvejournals.com/article/15369/pdf

[8] Narayan, S. R. K. K. B. (2018). Pushover analysis – result borders due to hinge formation orders. Structural Monitoring and Maintenance, 5(2), 173. https://doi.org/10.12989/smm.2018.5.2.173

[9] Neal, B. G. (1977). The plastic Methods of Structural analysis. Taylor & Francis.

[10] Zienkiewicz, O. C. (1977). The finite element method.

[11] Chen, W. F., & Han, D. (1988). Plasticity for structural engineers. Springer.

[12] Cook, R. D., Malkus, D. S., Plesha, M. E., & Witt, R. J. (2007). Concepts and Applications of Finite Element Analysis (5th ed.). John Wiley & Sons.

[13] Belytschko, T., Liu, W. K., Moran, B., & Elkhodary, K. (2014). Nonlinear finite elements for continua and structures. John Wiley & Sons.

[14] Newmark, N. M., & Hall, W. J. (1975). Seismic Design Criteria for Nuclear Reactor Facilities. -, 757–770. https://cedb.asce.org/CEDBsearch/record.jsp?dockey=0282559

[15] Yancey, C. W. C. (1980). Review and refinement of ATC 3-06 tentative seismic provisions : https://doi.org/10.6028/nbs.ir.80-2111-7

[16] Priestley, M. J. N., Calvi, G. M., & Kowalsky, M. J. (2007). Displacement-based seismic design of structures. Iuss Press.

[17] Elnashai, A. S., & Di Sarno, L. (2008). Fundamentals of Earthquake Engineering. https://doi.org/10.1002/9780470024867

[18] Chopra, A. K. (2015). Dynamics of Structure eBook, Global Edition. Pearson Higher Ed.

[19] Türk Standartları Enstitüsü. (1997). TS 498: Yapı Elemanlarının Boyutlandırılmasında Alınacak Yüklerin Hesap Değerleri

[20] Afet ve Acil Durum Yönetimi Başkanlığı (AFAD). (2018). Türkiye Bina Deprem Yönetmeliği (TBDY 2018). Ankara, Türkiye: AFAD.

[21] Türk Standartları Enstitüsü (TSE). (2000). TS 500: Betonarme yapıların tasarım ve yapım kuralları. Ankara, Türkiye: TSE.

[22] Mander, J. B., Priestley, M. J. N., & Park, R. (1988). Theoretical Stress-Strain model for confined concrete. Journal of Structural Engineering, 114(8), 1804–1826. https://doi.org/10.1061/(asce)0733-9445(1988)114:8(1804)

APPENDIX A.

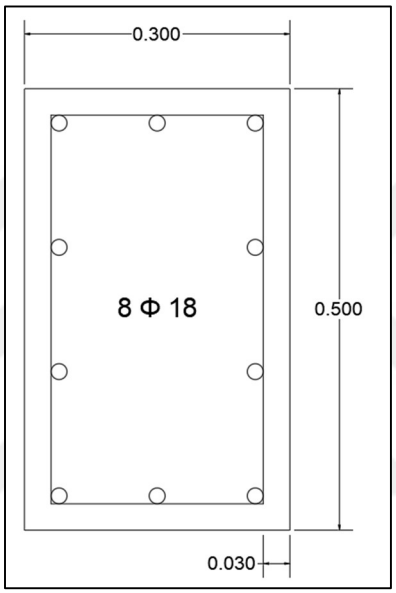

Figure 0.1: Section C1 Dimensions and reinforcement

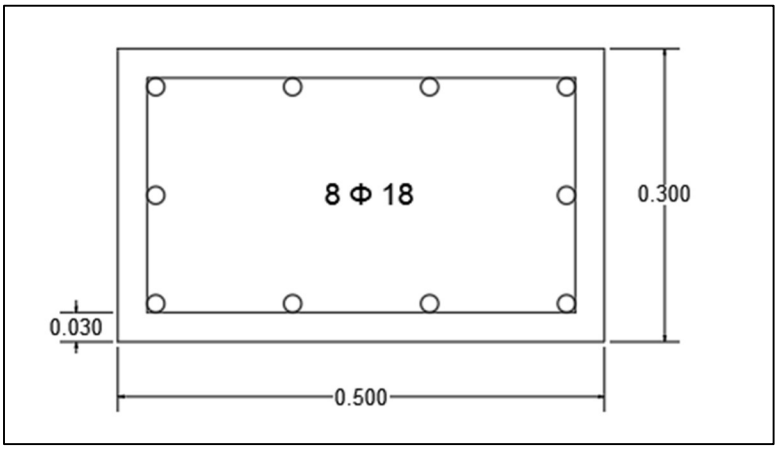

Figure A.2: Section C2 Dimensions and reinforcement

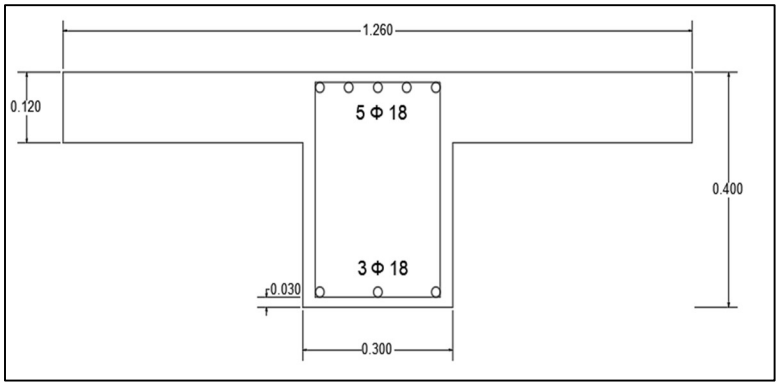

Figure 0.3: Section A Dimensions and reinforcement

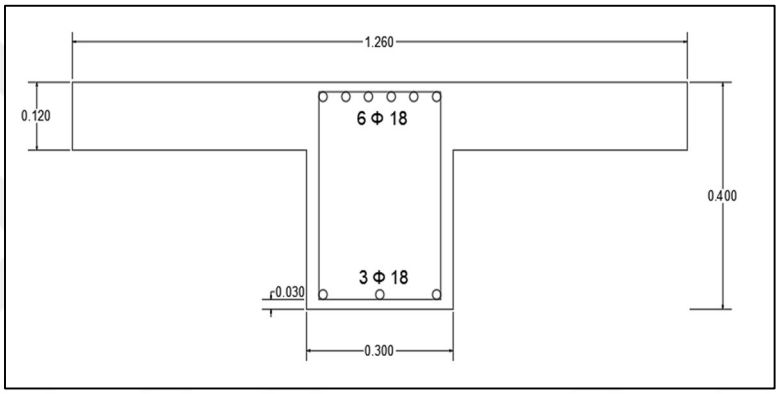

Figure 0.4: Section B Dimensions and reinforcement

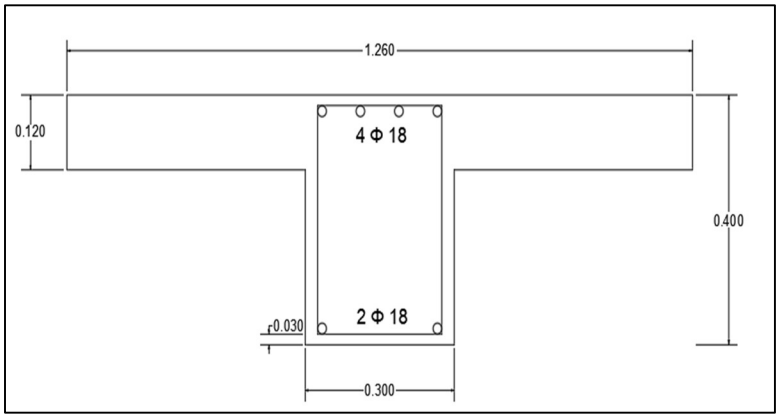

Figure 0.5: Section C Dimensions and reinforcement

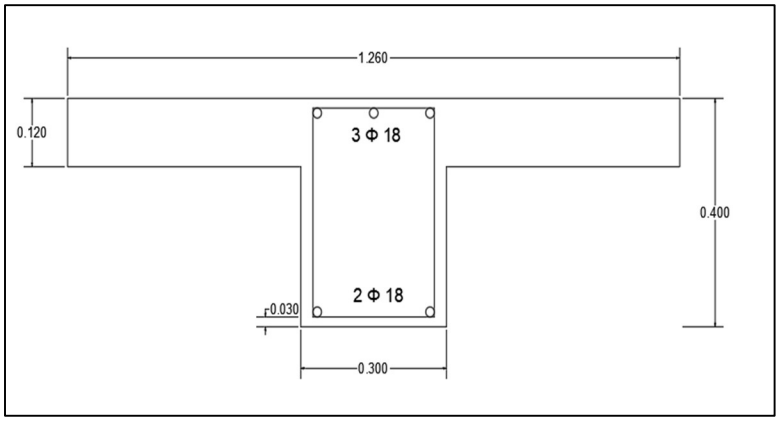

Figure 0.6: Section D Dimensions and reinforcement

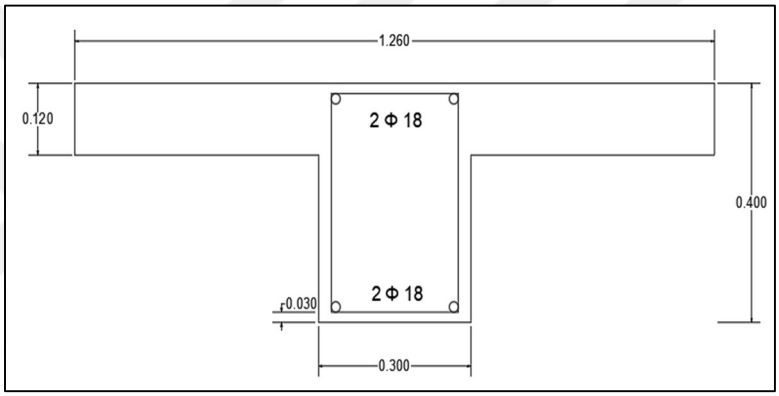

Figure A.7: Section E Dimensions and reinforcement

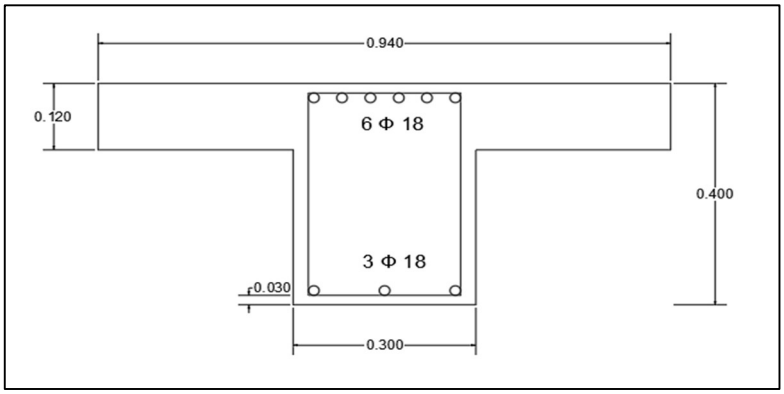

Figure 0.8: Section F Dimensions and reinforcement

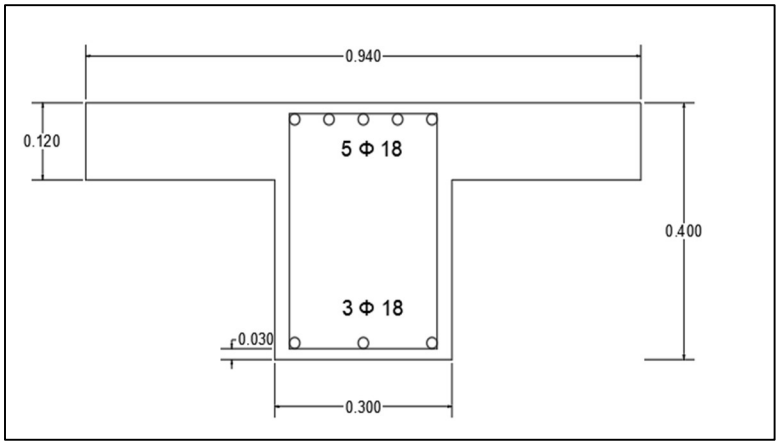

Figure 0.9: Section G Dimensions and reinforcement

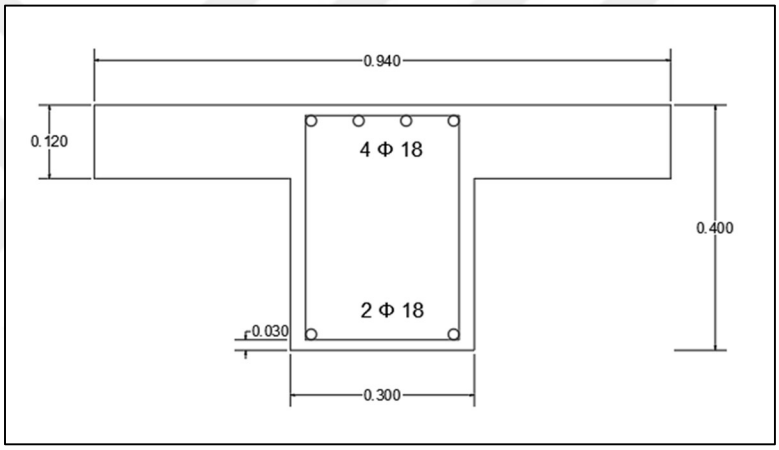

Figure 0.10: Section H Dimensions and reinforcement

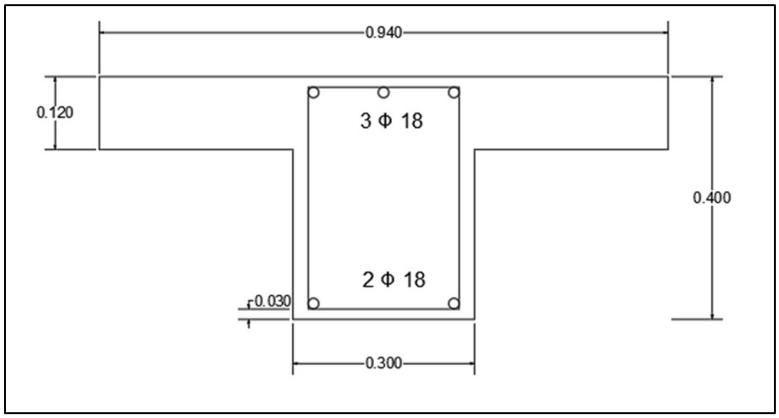

Figure 0.11: Section I Dimensions and reinforcement

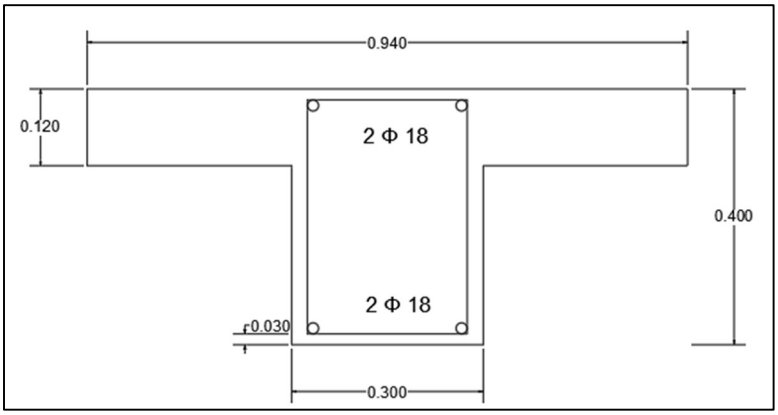

Figure A.12: Section J Dimensions and reinforcement

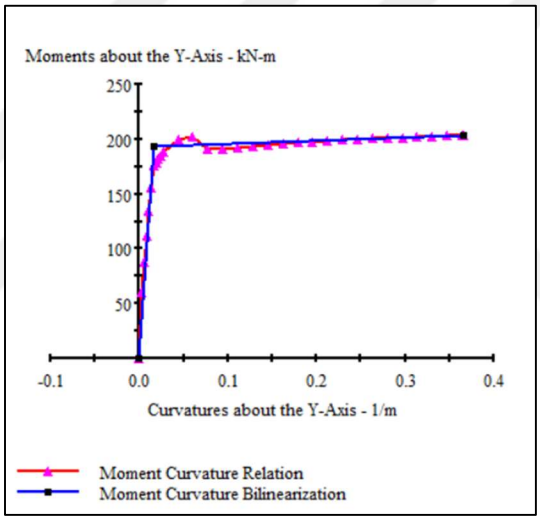

Figure 0.13: Section C1 story 1 moment curvature relationshop

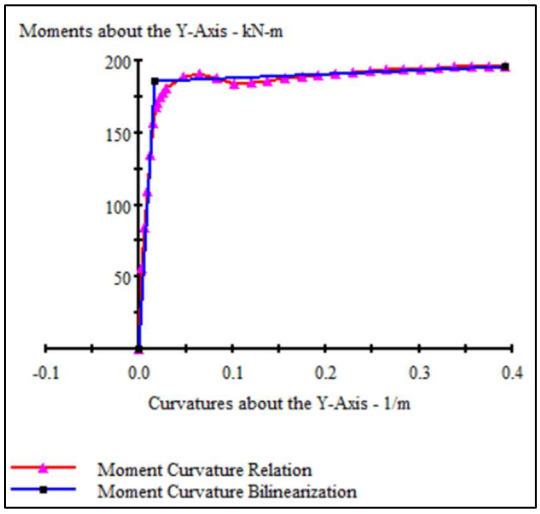

Figure 0.14: Section C2 story 2 moment curvature relationship

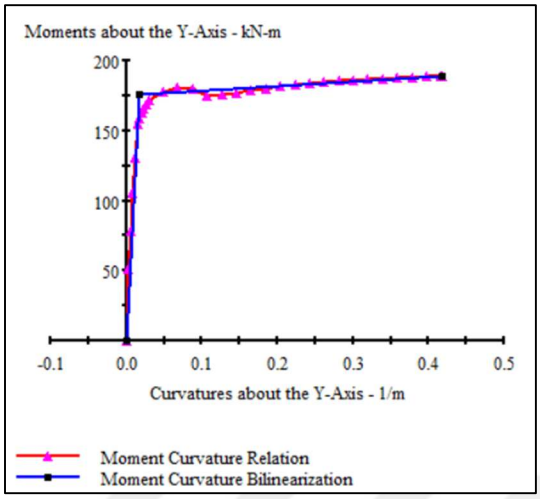

Figure A.15: Section C3 story 3 moment curvature relationship

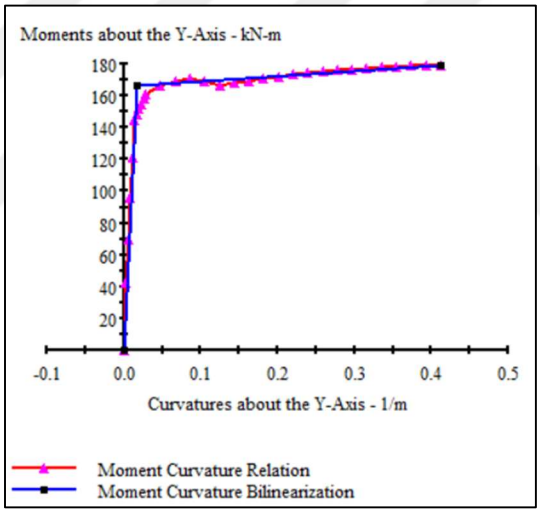

Figure 0.16: Section C4 story 4 moment curvature relationship

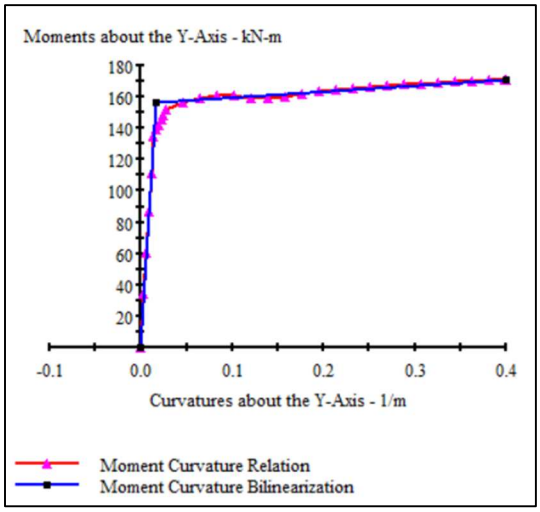

Figure A.17: Section C5 story 5 moment curvature relationship

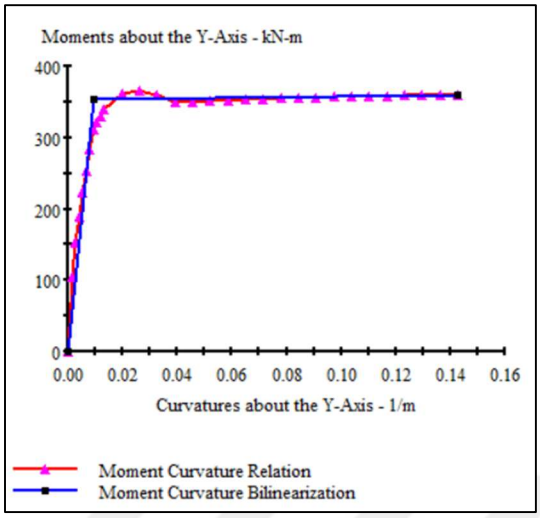

Figure 0.18: Section C2 story 1 moment curvature relationship

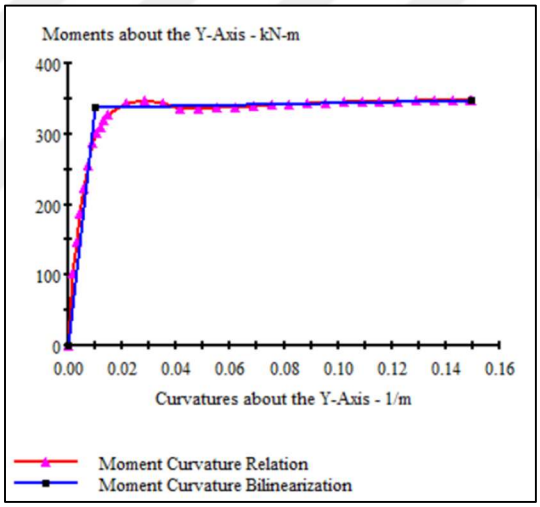

Figure A.19: Section C2 story 2 moment curvature relationship

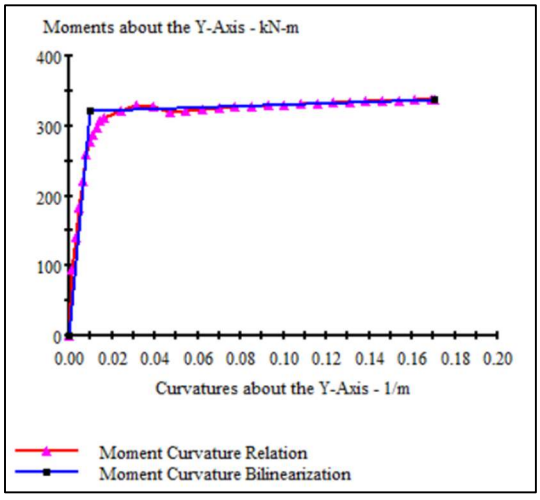

Figure 0.20: Section C2 story 3 moment curvature relationship

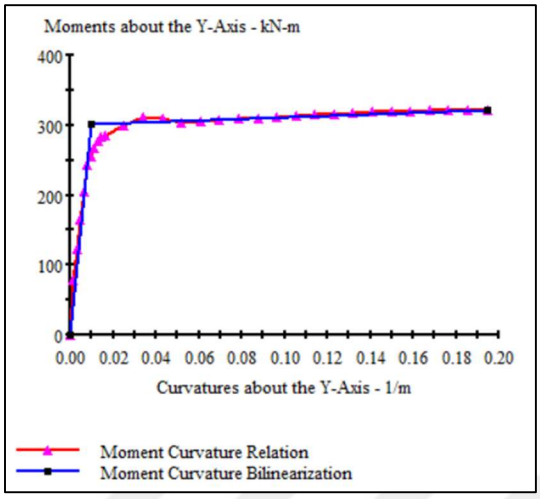

Figure A.21: Section C2 story 4 moment curvature relationship

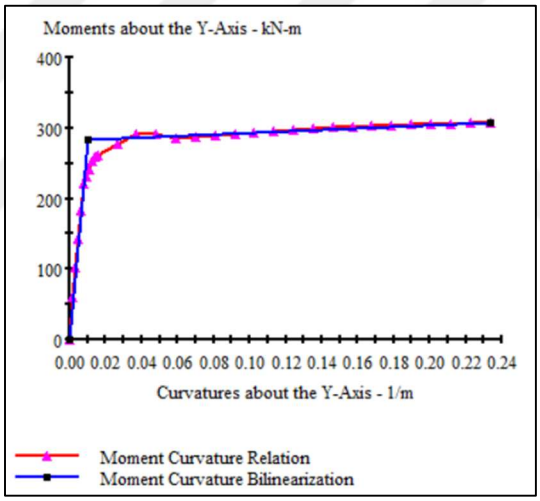

Figure A.22: Section C2 story 5 moment curvature relationship

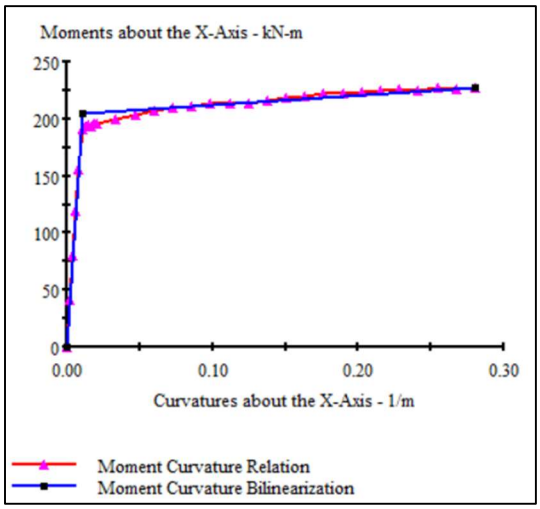

Figure A.23: Section A moment curvature relationship

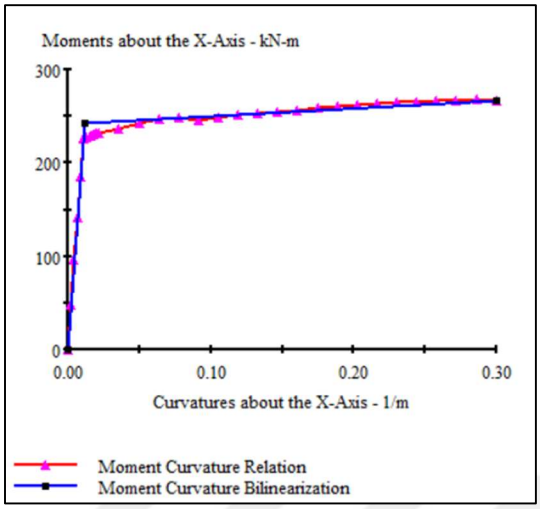

Figure A.24: Section B moment curvature relationship

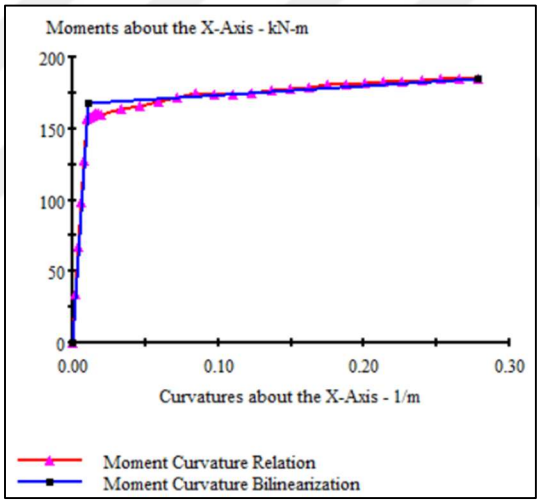

Figure A.25: Section C moment curvature relationship

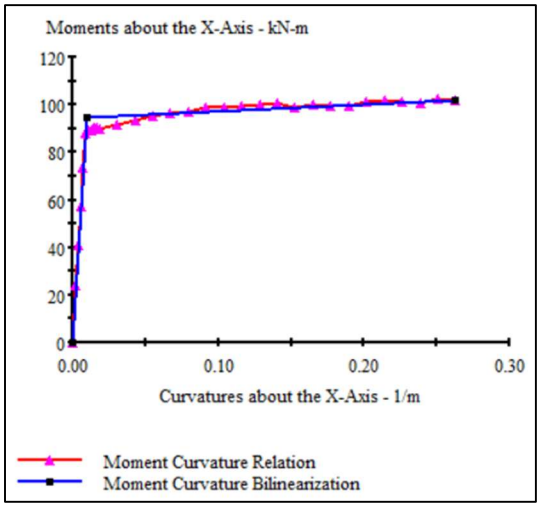

Figure 0.26: Section E moment curvature relationship

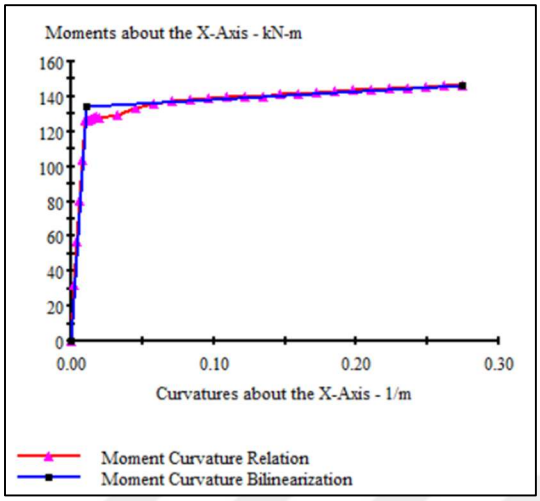

Figure 0.27: Section F moment curvature relationship

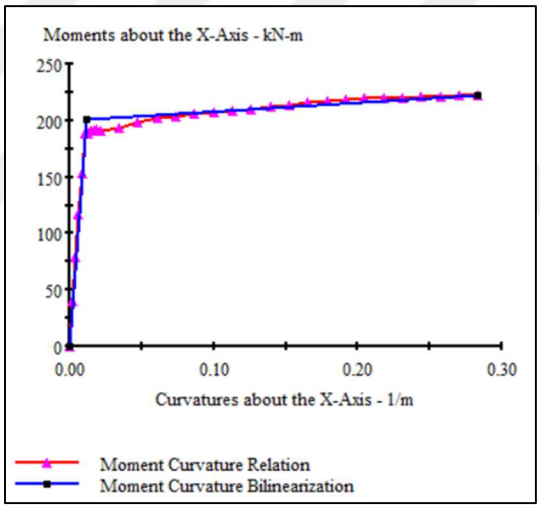

Figure A.28: Section G moment curvature relationship

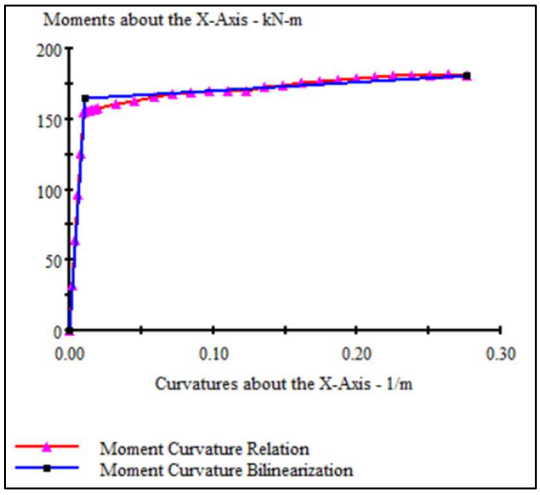

Figure 0.29: Section H end moment curvature relationship

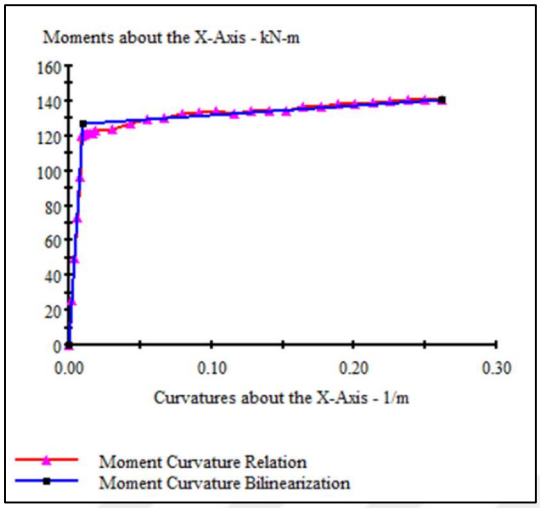

Figure A.30: Section I end moment curvature relationship

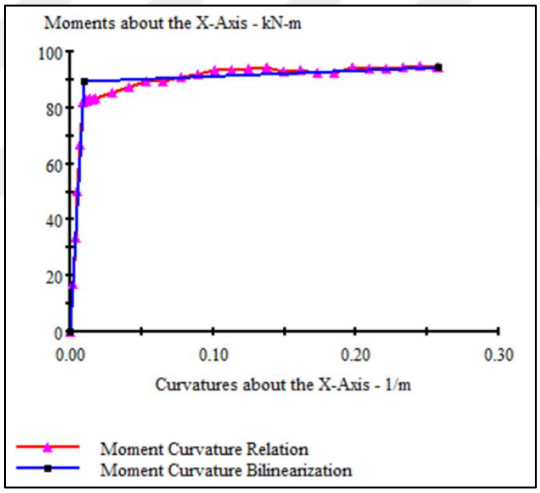

Figure A.31:Section J end moment curvature relationship